Contrib Mineral Petrol (2012) 163:277–296
DOI 10.1007/s00410-011-0672-x

ORIGINAL PAPER

The high PT stability of apatite and Cl partitioning between apatite and hydrous potassic phases in peridotite: an experimental study to 19 GPa with implications for the transport of P, Cl and K in the upper mantle

Jürgen Konzett · Dieter Rhede · Daniel J. Frost

Received: 14 December 2010 / Accepted: 6 July 2011 / Published online: 27 July 2011

Abstract High PT experiments were performed in the range 2.5–19 GPa and 800–1,500°C using a synthetic peridotite doped with trace elements and OH-apatite or with Cl-apatite + phlogopite. The aim of the study was (1) to investigate the stability and phase relations of apatite and its high PT breakdown products, (2) to study the compositional evolution with P and T of phosphate and coexisting silicate phases and (3) to measure the Cl-OH partitioning between apatite and coexisting calcic amphibole, phlogopite and K-richterite. Apatite is stable in a garnet-lherzolite assemblage in the range 2.5–8.7 GPa and 800–1,100°C. The high-P breakdown product of apatite is tuite γ-$Ca_3(PO_4)_2$, which is stable in the range 8–15 GPa and 1,100–1,300°C. Coexisting apatite and tuite were observed at 8 GPa/1,050°C and 8.7 GPa/1,000°C. MgO in apatite increases with P from 0.8 wt% at 2.5 GPa to 3.2 wt% at 8.7 GPa. Both apatite and tuite may contain significant Na, Sr and REE with a correlation indicating 2 Ca^{2+}=Na^{+} + REE^{3+}. Tuite has always higher Sr and REE and lower Fe and Mg than apatite. Phosphorus in the peridotite phases decreases in the order $P_{melt} \gg P_{grt} \gg P_{Mg2SiO4} > P_{cpx} > P_{opx}$. The phosphate-saturated P_2O_5 content of garnet increases from 0.07 wt% at 2.5 GPa to 1.5 wt% at 12.8 GPa. Due to the low bulk Na content of the peridotite, $^{[8]}Na^{[4]}P^{[8]}M^{2+}{}_{-1}{}^{[4]}Si_{-1}$ only plays a minor role in controlling the phosphorus content of garnet. Instead, element correlations indicate a major contribution of $^{[6]}M^{2+[4]}P^{[6]}M^{3+}{}_{-1}{}^{[4]}Si_{-1}$. Pyroxenes contain ~200–500 ppm P and olivine has 0.14–0.23 wt% P_2O_5 in the P range 4–8.7 GPa without correlation with P, T or X_{Mg}. At ≥12.7 GPa, all Mg_2SiO_4 polymorphs have <200 ppm P. Coexisting olivine and wadsleyite show an equal preference for phosphorus. In case of coexisting wadsleyite and ringwoodite, the latter fractionates phosphorus. Although garnet shows by far the highest phosphorus concentrations of any peridotite silicate phase, olivine is no less important as phosphorus carrier and could store the entire bulk phosphorus budget of primitive mantle. In the Cl-apatite + phlogopite-doped peridotite, apatite contains 0.65–1.35 wt% Cl in the PT range 2.5–8.7 GPa/800–1,000°C. Apatite coexists with calcic amphibole at 2.5 GPa, phlogopite at 2.5–5 GPa and K-richterite at 7 GPa, and all silicates contain between 0.2 and 0.6 wt% Cl. No solid potassic phase is stable between 5 and 8.7 GPa. Cl strongly increases the solubility of K in hydrous fluids. This may lead to the breakdown of phlogopite and give rise to the local presence in the mantle of fluids strongly enriched in K, Cl, P and incompatible trace elements. Such fluids may get trapped as micro-inclusions in diamonds and provide bulk compositions suitable for the formation of unusual phases such as KCl or hypersilicic Cl-rich mica.

Keywords Apatite · High pressure · Peridotite · Cl-OH partitioning

Communicated by T. L. Grove.

J. Konzett (✉)
Institute of Mineralogy and Petrology,
University of Innsbruck, Innrain 52,
6020 Innsbruck, Austria
e-mail: juergen.konzett@uibk.ac.at

D. Rhede
GFZ German Research Centre for Geosciences,
Telegraphenberg, 14473 Potsdam, Germany

D. J. Frost
Bavarian Research Institute of Experimental Geochemistry
and Geophysics, University of Bayreuth,
95440 Bayreuth, Germany

Introduction

Apatite is the most abundant naturally occurring phosphate and one of the most important halogen-bearing minerals on Earth. As a widespread accessory or minor phase in virtually all igneous and metamorphic rocks, apatite carries an essential portion of the bulk phosphorus content of 0.1–0.3 wt% P_2O_5 of continental and oceanic crust (Rudnick and Gao 2003; Klein 2004). Apatite is also one of the major phosphates on the moon and the terrestrial planets (Patiño Douce and Roden 2006 and references therein) and is the only OH-bearing phase currently known from the moon. Most recently, it was shown that lunar apatite may contain up to several thousand ppm H_2O (McCubbin et al. 2010, Boyce et al. 2010). This finding indicates H_2O contents of the moon's interior several orders of magnitude higher than previously estimated and challenges currently accepted models for the formation and cooling of the moon. Water contents of up to 0.64 wt% were found in apatite from an SNC meteorite (Leshin 2000), making apatite an important water reservoir in the Martian interior. Because of its strongly incompatible behaviour in igneous processes, phosphorus together with Fe and Ti is concentrated during fractional crystallization, eventually resulting in the formation of apatite ± FeTi-oxide deposits (Kolker 1982). Apatite is not present in primitive terrestrial mantle rocks due to their low bulk phosphorus contents of 90–100 ppm (McDonough and Sun 1995; Workman and Hart 2005; Pearson et al. 2004; Palme and O'Neill 2004; McDonough 1990). However, it is frequently found in metasomatically altered peridotitic mantle and is often associated with phlogopite and/or calcic amphibole (e.g. Exley and Smith 1982; Zanetti et al. 1999; Wass et al. 1980; O'Reilly and Griffin 1988, 2000; Rudnick et al. 1993; Ionov et al. 1996, 2006). In these rocks, apatite carries a major portion of the whole rock LILE, HFSE and REE-budget (e.g. O'Reilly et al. 1991; O'Reilly and Griffin 2000; Exley and Smith 1982). Mantle apatite often contains high concentrations of U and Th. Hence, it was proposed that the presence of apatite may critically influence the heat production in metasomatically altered mantle (O'Reilly and Griffin 2000). The noble gas isotopic composition of apatite was used to place constraints on the source of metasomatizing fluids beneath south-eastern Australia (Matsumoto et al. 1997). The formation of apatite is often ascribed to the interaction of mantle rocks with small volumes of phosphorus-rich carbonatitic melts or fluids (Rudnick et al. 1993; Hauri et al. 1993; Morishita et al. 2003). In rare instances, vestiges of these metasomatic agents are preserved as frozen grain boundary melts (Rosenbaum et al. 1997; Zhang et al. 2007) or as fluid/melt inclusions in diamond typically associated with apatite and K–Cl-LILE-rich phases (Lang and Walmsley 1983; Guthrie et al. 1991; Tomlinson et al. 2005; Titkov et al. 2006; Klein-BenDavid et al. 2006; Wirth et al. 2009). Partial melting of deep-seated apatite ± phlogopite-bearing asthenospheric or lithospheric mantle rocks may lead to the formation of kimberlites and lamproites (Foley 1992). Apatite is the major solid Cl carrier in the mantle because hydrous silicates with extremely rare exceptions do not incorporate significant Cl due to Fe–Cl avoidance (Volvinger et al. 1985; Kullerud 1995; Oberti et al. 1993) and strong partitioning of Cl into fluids. Therefore, the breakdown of apatite contributes to the high percentage of Cl recycled in subduction zones (Straub and Layne 2003). Nevertheless, partitioning of Cl between apatite and hydrous silicates provides a potential mechanism to avoid shallow-level recycling and to transport at least small amounts of Cl to transition zone depths. Although mantle apatite may be rich in F, its overall importance as F carrier in the mantle is negligible. This is because F unlike Cl is strongly compatible, shows a crystal chemical affinity to Mg-rich hydrous silicates and can also substitute into the olivine structure (Bromiley and Kohn 2007). These factors contribute to the low recycling efficiency of F compared to Cl in subduction zones (Straub and Layne 2003). The high-P solid-state breakdown product of apatite is tuite [γ-$Ca_3(PO_4)_2$], which was found in shocked chondritic and SNC meteorites (Xie et al. 2003; Ozawa et al. 2007; Greshake and Fritz 2009). Experiments by Murayama et al. (1986) have shown that pure OH- and F-apatite break down at 11–13 GPa between 1,000 and 1,500°C with a negative slope of the apatite–tuite phase boundary and a slightly lower ($\leq$1 GPa) upper P stability limit of the OH-endmember. Due to the large spacing of experimental data points, however, no reasonable comparison of the upper T stability limits of OH- and F-apatite is possible. In MORB-type bulk compositions, tuite forms at P $\geq$ 7.5 GPa by reactions involving garnet and SiO_2 (Konzett and Frost 2009). Like apatite, tuite contains large and high-coordinated lattice positions and, hence, is an eminently suitable host for LIL elements (Sugiyama and Tokonami 1987; Konzett and Frost 2009). Whereas apatite is by far the most important subsolidus carrier of phosphorus under crustal PT conditions, silicates—in particular garnet—start to become additional storage sites of phosphorus at P $\geq$ 3 GPa in a wide range of bulk compositions (e.g. Thompson 1975; Brunet et al. 2006; Konzett et al. 2008; Konzett and Frost 2009). The increasing phosphorus solubility in garnet may lead to a disappearance of apatite from garnet-bearing high-P rocks.

This study was undertaken to contribute to a better understanding of phosphorus and chlorine transport and storage in the upper mantle and transition zone. Its major aims are as follows: (1) to investigate the PT stability of OH- and Cl-apatite and its high-P breakdown product tuite in a representative upper mantle peridotite bulk composition, (2)

to explore the phosphorus storage capacity of the peridotite silicate phases—in particular of garnet and the Mg_2SiO_4 polymorphs and (3) to place constraints on the mechanisms of upper mantle transport and storage of Cl by studying the PT stability of Cl-apatite and the partitioning of Cl between apatite, phlogopite and amphibole.

Experimental and analytical techniques

Four bulk compositions were used in this study, and all are based on a moderately fertile spinel lherzolite from Mont Briançon, French Massif Central, modified by subtraction of 30 wt% olivine (Fo_{91}) and addition of 0.4 wt% Na_2O (modBRIAN2; cf. Konzett and Ulmer 1999; Fumagalli et al. 2009). Bulk composition I consists of modBRIAN2 doped with 3 wt% synthetic hydroxyl apatite and a trace element mix containing Nb, Ta, Zr, Y, Ba, Sr, Rb, Ce, Nd and Lu with concentrations between 250 and 350 ppm (cf. Konzett and Frost 2009); bulk composition II consists of modBRIAN2 doped with 5 wt% synthetic Cl-apatite + 5 wt% synthetic phlogopite + trace element mix; bulk composition IIa corresponds to bulk composition II without any trace elements added and bulk composition III consists of modBRIAN2 doped with 5 wt% Cl-apatite + 15 wt% phlogopite + trace element mix (Table 1). Modified BRIAN2 was prepared from high-purity (≥99.9%) and finely ground SiO_2, TiO_2, Cr_2O_3, MgO, NiO, $CaCO_3$ and Na_2CO_3 by mixing in ethanol for 20 min and stepwise decarbonation to 800°C with intermittent checks of the loss on ignition. Al, Fe^{2+} and Mn^{2+} were added as γ-Al_2O_3, Fe_2SiO_4 and MnO. Phlogopite was synthesized in an externally heated pressure vessel at 0.3 GPa/680°C from an oxide–carbonate mix, and Cl-apatite was prepared following the method of Bauer and Klee (1993) from ammonium dihydrogen phosphate and calcium chloride. This synthesis yielded clear idiomorphic apatite crystals of up to 4 × 0.5 mm in size. Electron microprobe analysis yields P_2O_5 41.6 ± 0.2; CaO 54.7 ± 0.5; and Cl 6.9 ± 0.1 ($n = 15$) corresponding to pure Cl-apatite. The experiments on Cl partitioning between apatite, phlogopite and amphibole faced two difficulties: Cl-loss from apatite and strongly enhanced fluid solubility of K in the presence of Cl. Although the starting materials were permanently stored at 150°C, trace amounts of free water are present during the experiments. The source of water is moisture from the air adsorbed to the starting material (Médard et al. 2008) and breakdown of phlogopite due to high potassium solubility in the free fluid. As a result of its extreme fluid compatibility, a large portion of Cl was lost from the Cl-apatite by Cl ⇔ OH exchange with the fluid (Table 2). The very high K-solubility in the Cl-rich fluid led to a complete disappearance of hydrous potassic phases from the experimental assemblages in bulk compositions II and IIa between 7 and 8.7 GPa. In order to avoid any potential effect of trace elements on the availability of K for hydrous potassic silicate stability, the experiment at 7 GPa/1,000°C was repeated with bulk composition IIa. This, however, had no effect on the phase assemblage. It was only after increasing the bulk K_2O content of the starting material from 0.5 to 1.4 wt% that K-richterite was stabilized at 7 GPa/800°C.

Table 1 The composition of the starting materials

Bulk no.	I	II (a)	III
SiO_2	44.2	43.3	43.3
TiO_2	0.1	0.1	0.1
Al_2O_3	3.8	4.1	4.8
Cr_2O_3	0.7	0.6	0.6
FeO	7.1	6.6	6.1
MnO	0.1	0.1	0.1
MgO	36.5	35.5	35.0
NiO	0.2	0.2	0.2
CaO	5.3	5.8	5.4
Na_2O	0.7	0.7	0.6
K_2O	–	0.5	1.4
P_2O_5	1.2	1.9	1.7
H_2O	0.1	0.2	0.5
Cl	–	0.3	0.3
∑	100.0	100.0	100.0

I: modified BRIAN-2 + 3% OH-apatite (cf Konzett and Ulmer 1999)

II: modified BRIAN-2 + 5% Cl-apatite + 5% phlogopite

IIa: corresponds to bulk II without trace elements added

III: modified BRIAN-2 + 5% Cl-apatite + 15% phlogopite

Experiments (Table 3) were performed with 500t and 1000t multi-anvil presses at the Institute of Mineralogy and Petrology, University of Innsbruck (UI), and the Bavarian Research Institute of Experimental Geochemistry and Geophysics, University of Bayreuth (BGI), respectively, under conditions outlined in detail in Konzett and Frost (2009).

The composition of phases was analysed with a JEOL 8600 superprobe, and the identity of Mg_2SiO_4 polymorphs was verified using laser Raman spectroscopy. Variable beam currents and measurement times of the X-ray lines were used dependent on the phases analysed and the concentration of the elements measured. Quenched melt, apatite, phlogopite and calcic amphibole were analysed with 5 nA beam current in order to minimize Cl- and alkali diffusion and/or because most grains were too small to be analysed with a beam in raster mode. Resulting 2σ uncertainties for Cl in an individual analysis are 4–7% for apatite, 8–12% for phlogopite and 12% for calcic amphibole. The low X-ray count rates obtained with 5 nA also yielded comparatively high 2σ uncertainties for Sr, Ce and Nd of ~30, 25 and 20%, respectively (cf. Table 2).

Table 2 Representative and averaged analyses of apatite and tuite, garnet, phlogopite, Ca-amphibole and K-richterite, Mg_2SiO_4 polymorphs, pyroxenes, quenched melt

Apatite and tuite

Run # (bulk)	B05-17 (I)	JKI-98 (IIa)	MA31 (II)	MA21 (II)	MA50 (II)	B07-9 (II)	MA46 (II)	B07-11 (I)	B07-1 (I)	MA46 (II)
P[GPa]/T[°C]	8/1,050	2.5/900	4/1,000	5/1,000	7/1,000	7.5/1,000	8.7/1,000	8/1,100	9/1,100	8.7/1,000
Phase	ap	ap	ap	ap	ap	ap	ap	tu	tu	tu
# of analyses	1	5	8	5	17	8	7	1	7	4
P_2O_5	41.23 (95)	42.50 (53)	42.11 (32)	41.44 (33)	41.99 (53)	41.50 (78)	42.17 (36)	43.47 (98)	44.29 (34)	44.81 (26)
SiO_2	0.27 (04)	nd	0.17 (07)	0.18 (03)	0.08 (07)	0.25 (12)	0.14 (04)	0.18 (05)	0.14 (02)	0.20 (01)
CaO	47.98 (50)	55.29 (28)	52.18 (80)	51.08 (49)	50.33 (75)	48.45 (80)	51.05 (64)	44.29 (46)	45.97 (77)	50.17 (66)
SrO	0.51 (14)		0.75 (12)	0.75 (10)	0.54 (10)	0.64 (16)	0.34 (11)	1.29 (20)	1.05 (05)	1.32 (08)
FeO_{tot}	1.40 (25)	0.41 (11)	0.69 (14)	0.50 (18)	0.94 (13)	0.80 (17)	1.08 (09)	<0.05	0.12 (07)	0.32 (05)
MnO	<0.05	<0.05	<0.05	<0.05	<0.05	<0.05	<0.05	<0.05	<0.05	<0.05
MgO	3.60 (15)	0.75 (03)	1.67 (08)	1.85 (06)	2.46 (20)	3.06 (08)	2.92 (19)	0.16 (05)	0.11 (03)	0.14 (02)
Ce_2O_3	0.54 (13)		0.75 (19)	0.80 (17)	0.48 (20)	0.82 (36)	0.08 (07)	4.27 (24)	3.42 (41)	0.94 (39)
Nd_2O_3	0.73 (13)		0.75 (18)	0.74 (16)	0.37 (17)	0.62 (25)	0.07 (05)	3.55 (22)	2.95 (33)	0.69 (29)
Na_2O	0.31 (05)	<0.05	0.26 (06)	0.19 (05)	0.06 (05)	0.13 (07)	0.11 (05)	1.61 (10)	1.34 (11)	0.52 (11)
Cl	0.39 (05)	0.99 (02)	0.65 (07)	1.35 (10)	2.35 (12)	2.21 (21)	1.21 (22)			
H_2O^a	1.67	1.56 (01)	1.63 (02)	1.42 (04)	1.19 (04)	1.20 (06)	1.49 (07)			
$\sum$	98.63	101.56 (68)	101.61 (65)	100.31 (58)	100.82 (81)	99.53 (67)	100.67 (87)	98.98	99.40 (44)	99.03 (56)
$-Cl = O$	0.09	0.22 (00)	0.15 (01)	0.31 (02)	0.53 (03)	0.50 (05)	0.27 (05)			
$\sum$	98.54	101.33 (68)	101.46 (64)	100.00 (56)	100.29 (82)	99.03 (66)	100.40 (89)			

Garnet

Run # (bulk)	B06-19 (I)	B06-13 (I)	B06-11 (I)	B07-11 (I)	B05-10 (I)	B07-1 (I)	B07-4 (I)	B07-2 (I)	B06-16 (I)
P[GPa]/T[°C]	6/1,100	6/1,300	6/1,500	8/1,100	8/1,200	9/1,100	9/1,300	12.8/1,200	15/1,500
# of analyses	10	11	11	8	12	9	7	5	9
SiO_2	41.80 (38)	43.16 (26)	43.20 (24)	40.94 (20)	42.83 (39)	42.08 (34)	43.09 (47)	42.20 (38)	46.13 (50)
TiO_2	0.21 (07)	0.29 (04)	0.26 (05)	0.24 (06)	0.32 (06)	0.24 (03)	0.34 (09)	0.18 (04)	0.18 (03)
Al_2O_3	23.24 (82)	20.79 (15)	20.78 (88)	22.29 (46)	20.79 (47)	21.54 (26)	21.10 (40)	20.75 (87)	14.77 (79)
Cr_2O_3	1.07 (32)	3.31 (26)	3.12 (64)	0.97 (14)	2.12 (25)	1.37 (24)	1.63 (34)	0.47 (16)	0.94 (15)
P_2O_5	0.78 (09)	0.60 (22)	0.62 (19)	1.39 (09)	1.00 (14)	1.33 (12)	1.30 (16)	1.50 (14)	1.59 (06)
FeO_{tot}	6.01 (74)	1.67 (75)	2.42 (76)	7.48 (54)	4.80 (72)	6.73 (25)	4.07 (13)	5.91 (40)	5.25 (16)
MnO	0.21 (07)	0.15 (03)	0.10 (06)	0.27 (06)	0.21 (06)	0.26 (04)	0.19 (04)	0.29 (05)	0.16 (05)
MgO	22.22 (51)	24.94 (52)	24.88 (53)	20.67 (45)	24.04 (64)	22.05 (25)	24.468 (24)	19.40 (36)	24.64 (71)
CaO	4.68 (23)	5.33 (26)	5.03 (18)	5.00 (34)	4.89 (24)	5.05 (32)	4.83 (22)	8.09 (42)	6.62 (17)
Na_2O	0.17 (03)	0.07 (02)	0.07 (02)	0.26 (03)	0.16 (01)	0.26 (02)	0.21 (02)	0.48 (06)	0.22 (01)
$\sum$	100.39 (72)	100.31 (41)	100.50 (42)	99.50 (40)	101.16 (41)	100.91 (42)	101.21 (65)	99.27 (49)	100.50 (73)

Table 2 continued

Garnet							
Run # (bulk) P[GPa]/T[°C] # of analyses	B08-5 (I) 19/1,200 10	JKI-98 (IIa) 2.5/900 6	MA31 (II) 4/1,000 14	MA21 (II) 5/1,000 6	MA50 (II) 7/1,000 5	B07-9 7.5/1,000 6	MA46 (II) 8.7/1,000 11
SiO_2	48.12 (99)	42.04 (17)	42.61 (29)	41.87 (35)	41.88 (85)	42.28 (51)	41.67 (28)
TiO_2	0.14 (06)	0.19 (03)	0.14 (05)	0.16 (03)	0.09 (03)	0.10 (03)	0.18 (06)
Al_2O_3	0.71 (212)	22.27 (58)	23.52 (56)	24.03 (91)	23.86 (63)	23.70 (84)	22.87 (61)
Cr_2O_3	0.97 (19)	1.98 (46)	0.98 (40)	0.88 (44)	0.44 (15)	0.66 (31)	0.79 (30)
P_2O_5	1.47 (22)	0.07 (01)	0.26 (09)	0.34 (05)	1.06 (27)	0.91 (22)	1.12 (13)
FeO_{tot}	4.47 (22)	8.14 (34)	7.05 (22)	6.58 (51)	7.29 (31)	6.78 (75)	7.80 (19)
MnO	0.16 (05)	0.42 (03)	0.23 (07)	0.27 (07)	0.20 (05)	0.22 (04)	0.23 (06)
MgO	25.30 (84)	18.52 (17)	21.94 (34)	21.58 (75)	21.95 (32)	22.33 (53)	20.98 (25)
CaO	7.33 (54)	7.03 (25)	4.59 (28)	4.60 (25)	3.91 (39)	3.82 (24)	4.74 (20)
Na_2O	0.32 (04)	0.03 (02)	0.08 (01)	0.11 (02)	0.17 (03)	0.21 (03)	0.26 (03)
$\sum$	98.98 (40)	100.68 (58)	101.40 (41)	100.41 (67)	100.85 (59)	100.25 (44)	100.64 (40)

Phlogopite, Ca-amphibole and K-richterite					
Run # (bulk) P[GPa]/T[°C] # of analyses	JKI-98 (IIa) 2.5/900 3	MA31 (II) 4/1,000 10	MA21 (II) 5/1,000 7	JKI-98 (IIa) 2.5/900 4	MA55 (III) 7/800 8
SiO_2	40.63 (33)	41.89 (82)	42.05 (99)	45.55 (73)	55.34 (53)
TiO_2	0.43 (05)	0.49 (19)	0.36 (10)	0.46 (07)	0.05 (04)
Al_2O_3	14.50 (88)	13.62 (54)	12.12 (40)	11.95 (75)	0.74 (12)
Cr_2O_3	0.82 (13)	0.29 (05)	0.32 (08)	1.77 (14)	0.07 (04)
FeO_{tot}	2.73 (09)	2.71 (42)	2.09 (105)	2.80 (07)	4.80 (50)
MnO	<0.05	<0.05	<0.05	<0.05	<0.05
MgO	25.56 (87)	25.30 (54)	27.80 (124)	19.61 (20)	20.98 (71)
CaO	<0.05	0.15 (10)	0.14 (06)	11.13 (17)	5.73 (37)
Na_2O	1.04 (05)	0.23 (05)	0.18 (05)	2.97 (03)	3.57 (20)
K_2O	7.84 (22)	9.41 (48)	8.97 (43)	1.11 (12)	5.65 (17)
Cl	0.40 (08)	0.23 (05)	0.41 (05)	0.19 (05)	0.56 (07)
H_2O^b	4.11 (02)	4.18 (05)	4.14 (07)	2.06 (03)	1.95 (02)
$\sum$	98.08 (34)	98.53 (118)	98.45 (77)	99.69 (66)	99.47 (85)
–Cl=O	0.09 (02)	0.05 (01)	0.09 (01)	0.04 (01)	0.13 (02)
$\sum$	97.93 (37)	98.48 (118)	98.36 (77)	99.65 (66)	99.34 (84)

Table 2 continued

Mg_2SiO_4 polymorphs											
Run # (bulk)	MA31 (II)	B06-19 (I)	B06-13 (I)	B06-11 (I)	B07-11 (I)	B07-1 (I)	B07-4 (I)	B07-2 (I)	B07-2 (I)	B08-5 (I)	B08-5 (I)
P[GPa]/T[°C]	4/1,000	6/1,100	6/1,300	6/1,500	8/1,100	9/1,100	9/1,300	12.8/1,200	12.8/1,200	19/1,200	19/1,200
Phase	ol	ol	ol	ol	ol	ol	ol	ol	wad	wad	ring
# of analyses	7	3	11	10	4	6	7	7	8	1	1
SiO_2	42.19 (26)	41.44 (09)	42.69 (28)	42.61 (12)	41.54 (51)	42.05 (15)	41.91 (32)	41.34 (39)	39.72 (28)	40.38	40.28
FeO_{tot}	7.53 (73)	6.20 (26)	0.26 (06)	0.72 (09)	7.86 (39)	5.85 (24)	3.54 (51)	8.73 (15)	15.90 (23)	6.27	9.97
MnO	0.10 (02)	0.08 (02)	<0.05	<0.05	0.08 (02)	0.05 (04)	<0.05	<0.05	<0.05	0.07	0.06
MgO	52.03 (69)	52.04 (25)	57.05 (56)	56.52 (29)	49.60 (81)	53.22 (30)	54.96 (51)	49.85 (50)	43.66 (63)	50.81	48.80
NiO	nd	0.37 (01)	0.08 (02)	<0.05	0.36 (04)	0.40 (05)	0.16 (06)	0.33 (07)	0.63 (08)	0.41	0.62
$\sum$	101.85 (43)	100.38 (14)	100.27 (59)	100.17 (28)	99.62 (86)	101.79 (26)	100.80 (72)	100.57 (70)	100.06 (85)	98.27	99.88
X_{Mg}	0.925 (08)	0.937 (03)	0.997 (01)	0.993 (01)	0.918 (05)	0.942 (02)	0.965 (05)	0.911 (02)	0.830 (02)	0.935	0.897
ppm P	691 ± 117	872 ± 54	668 ± 67	668 ± 78	865 ± 75	756 ± 76	1,019 ± 273	143 ± 58[c]	125 ± 31[c]	70 ± 16[c]	181 ± 65[c]

pyroxenes									
Run # (bulk)	B06-19 (I)	B06-13 (I)		B06-11 (I)	B07-11 (I)	B07-1 (I)		B07-4 (I)	
P[GPa]/T[°C]	6/1,100	6/1,300		6/1,500	8/1,100	9/1,100		9/1,300	
Phase	cpx	cpx	opx	opx	cpx	cpx	opx	cpx	opx
# of analyses	5	3	8	9	5	3	8	3	6
SiO_2	55.93 (20)	56.18 (29)	58.41 (56)	58.19 (46)	55.91 (16)	56.52 (18)	58.88 (37)	56.36 (27)	58.60 (55)
TiO_2	0.16 (01)	0.07 (02)	0.08 (06)	<0.05	0.06 (03)	0.07 (01)	<0.05	0.06 (01)	<0.05
Al_2O_3	1.89 (29)	1.91 (05)	0.89 (05)	1.54 (12)	1.68 (09)	1.67 (12)	0.14 (02)	1.45 (14)	0.18 (01)
Cr_2O_3	0.96 (10)	0.95 (05)	0.31 (07)	0.36 (07)	0.83 (09)	0.93 (11)	0.07 (09)	0.69 (02)	0.06 (06)
FeO_{tot}	2.75 (34)	1.77 (88)	2.05 (150)	1.99 (113)	3.36 (27)	2.77 (29)	4.38 (30)	3.23 (03)	3.93 (29)
MnO	0.06 (05)	<0.05	<0.05	<0.05	<0.05	0.09 (02)	<0.05	<0.05	<0.05
MgO	18.38 (55)	20.42 (48)	36.71 (111)	35.83 (92)	18.09 (30)	17.92 (31)	36.81 (20)	20.93 (29)	36.85 (41)
CaO	18.43 (86)	18.25 (82)	1.18 (09)	2.02 (20)	18.65 (54)	19.42 (02)	0.26 (06)	16.12 (28)	0.50 (08)
Na_2O	1.82 (27)	1.34 (04)	0.19 (03)	0.30 (06)	1.85 (07)	1.94 (10)	0.07 (03)	1.41 (13)	0.06 (04)
$\sum$	100.36 (24)	100.89 (46)	99.84 (83)	100.28 (55)	100.57 (26)	101.33 (52)	100.63 (54)	100.33 (39)	100.20 (81)
ppm P	426 ± 16 [4][d]	334 ± 52 [4]	193 ± 14 [5]	212 ± 44 [7]	522 ± 86 [8]	481 ± 46 [5]	125/163[d]	352 ± 52 [5]	149 ± 56 [5]

Quenched melt		
Run # (bulk)	B06-13 (I)	B06-11 (I)
P[GPa]/T[°C]	6/1,300	6/1,500
# of analyses	5	8
SiO_2	3.64 (75)	4.58 (38)
TiO_2	0.38 (04)	0.36 (07)

Table 2 continued

Quenched melt		
Run # (bulk)	B06-13 (I)	B06-11 (I)
P[GPa]/T[°C]	6/1,300	6/1,500
# of analyses	5	8
Al_2O_3	0.27 (01)	0.21 (03)
Cr_2O_3	<0.05	<0.05
FeO_{tot}	0.13 (08)	0.33 (09)
MnO	0.09 (06)	<0.05
MgO	21.50 (75)	20.68 (18)
CaO	24.06 (78)	24.89 (32)
Na_2O	2.02 (66)	3.52 (19)
P_2O_5	7.58 (70)	8.14 (20)
SrO	nd	0.27 (06)
Ce_2O_3	nd	0.26 (07)
Nd_2O_5	nd	0.21 (11)
$\sum$	59.67 (208)	62.71 (32)

[a] Water calculated based on stoichiometric OH + Cl; numbers in brackets in columns 2 and 9 of the apatite and tuite analyses are typical 2σ-analytical uncertainties for an individual analysis; numbers in remaining columns are standard deviations of averaged analyses; Roman numbers next to run numbers refer to bulk compositions (cf. Table 1)

[b] Water calculated based on stoichiometric OH + Cl

[c] Phosphorus concentration of Mg_2SiO_4 polymorphs in B07-2 and B08-5 (Fig. 6) measured using fixed major element composition

[d] Numbers in square brackets give number of pyroxenes analysed for phosphorus

Table 3 Summary of experimental run conditions and products

Run no.	Bulk	Assembly	P[GPa]	T[°C]	Position[a]	Duration	Phases observed
B06-19	I	18/11	6.0	1,100	Upper	112 h 25 min	grt + cpx + opx + ol + **ap** (+mgs)
B06-13	I	18/11	6.0	1,300	Upper	80 h 10 min	grt + cpx + opx + ol + Q
B06-11	I	18/11	6.0	1,500	Upper	24 h 58 min	grt + opx + ol + Q
B05-17	I	18/11	8.0	1,050	Lower	186 h 07 min	grt + cpx + opx + ol + **ap** + **tu** (+mgs)
B07-11	I	18/11	8.0	1,100	Upper	97 h 00 min	grt + cpx + opx + ol + **tu** (+mgs)
B05-10	I	18/11	8.0	1,200	Lower	94 h 50 min	grt + cpx + opx + ol (+mgs)
B07-1	I	18/11	9.0	1,100	Upper	120 h 30 min	grt + cpx + opx + ol + **tu** (+mgs)
B07-4	I	18/11	9.0	1,300	Upper	72 h 05 min	grt + cpx + opx + ol (+mgs)
B07-2	I	14/8	12.8[b]	1,200		71 h 30 min	grt + cpx + opx + ol + wad + **tu** (+mgs)
B07-5	I	14/8	15.0	1,100		66 h 30 min	grt + cpx + opx + wad + **tu** (+mgs)
B06-16	I	14/8	15.0	1,500		24 h 30 min	grt + cpx + opx + wad
B08-5	I	10/5	19.0	1,200		71 h 20 min	grt + wad + ring
JKI-98	IIa	PC	2.5	900		457 h 00 min	grt + cpx + opx +ol + ap + phl + Cam
MA31	II	18/11	4.0	1,000	Lower	187 h 25 min	grt + cpx + opx +ol + phl + **ap**
MA21	II	18/11	5.0	1,000	Lower	145 h 30 min	grt + cpx + opx +ol + phl + **ap**
MA50	II	18/11	7.0	1,000	Lower	98 h 00 min	grt + cpx + opx +ol + **ap**
MA52	IIa	18/11	7.0	1,000	Upper	233 h 22 min	grt + cpx + opx +ol + **ap**
B07-9	II	18/11	7.5	1,000	Lower	144 h 38 min	grt + cpx + opx +ol + **ap**
MA46	II	18/11	8.7[b]	1,000	Lower	98 h 35 min	grt + cpx + opx +ol + **ap + tu**
MA55	III	18/11	7.0	800	Upper	261 h 30 min	grt + cpx + opx +ol + **ap** + Kr

Bold values represent the stability of different mineral phases

grt garnet, *cpx* clinopyroxene, *opx* orthopyroxene, *ol* olivine, *ap* apatite, *tu* tuite, *mgs* magnesite, *wad* wadsleyite, *ring* ringwoodite, *Q* quenched fluid/melt, *phl* phlogopite, *Cam* calcic amphibole, *Kr* K-richterite. Bulk compositions: see Table 1

[a] Refers to position of the charge in the MA assembly with respect to the thermocouple: u (upper) close to TC; l (lower) far from TC; *PC* piston cylinder; [b] experimental pressures tightly constrained by coesite–stishovite transition and by composition of coexisting olivine and wadsleyite

Phosphorus in the Mg_2SiO_4 polymorphs was analysed with 50 nA beam current and 50 s/25 s counting time on peak and background of the P-Kα line. Care was taken to measure only grains $\geq$10 μm in diameter and to avoid grains that show boundaries with garnet or Ca-phosphate. To assess the effect of secondary fluorescence from phosphorus on adjacent phases, compositional profiles were analysed across olivine grains with 15–20 μm diameter adjacent to Ca-phosphate grains. These profiles revealed a heterogeneous distribution of phosphorus concentrations and a sudden strong increase at distances of $\leq$3–5 μm from the olivine–Ca-phosphate grain boundary. This is in agreement with results obtained by Brunet and Chazot (2001). Phosphorus in pyroxenes was analysed using the analytical protocol described in Konzett and Frost (2009). At P > 9 GPa, the Mg_2SiO_4 polymorphs are too small to be analysed with a conventional electron gun. Instead, the JEOL electron microprobe JXA-8500F (Hyperprobe) equipped with a field emission gun at the GFZ German Research Centre for Geosciences Potsdam was used. Trace element measurements of phosphorus were taken with PET crystals using lower acceleration voltage and a liquid nitrogen trap to reduce the surface contamination. The analytical conditions included an acceleration voltage of 8 kV, a beam current of 30 nA and a focussed beam. The lower analytical sensitivity with decreasing acceleration voltage was compensated using three simultaneously working spectrometers. With this procedure, total counting times of 900 s (3*300 s) on the peak resulted in a reasonable detection limit of 10 ppm P. The background counting times were always set to half of the peak counting times. The CITZAF routine in the JEOL software, which is based on the $\Phi(\rho Z)$ method (Armstrong 1995), was used for data processing. Multiple measurements of different reference glasses (Brunet and Chazot 2001) were taken in order to check the reproducibility of the measurements.

Results

Textures and chemical homogeneity of the run products

All starting materials recrystallized to form euhedral to subhedral mineral grains with sizes between ~5 and ~20 μm in experiments at T $\leq$ 1,000°C in part showing well-equilibrated textures with 120° triple grain boundaries

(Fig. 1g). At higher temperatures, the grain size of garnet and orthopyroxene may increase to 50–100 μm. These larger grains often show numerous inclusions of other matrix phases, limiting the number of grains per experiment suitable for analysis. Apatite and tuite are present as lath-shaped to xenomorphic grains rarely exceeding 20 μm in diameter and also often containing inclusions (Figs. 1a, b). In many instances, the high density of inclusions and/or the small grain size made a reliable analysis difficult or even impossible. Highly variable SiO_2 and MgO concentrations were taken as indication of beam overlap with adjacent or included Mg- silicate phases, and these analyses were excluded from further considerations. Quenched melt forms layers of ≤20–30 μm thickness infiltrating the graphite liner at the end of the capsule close to the thermocouple (Fig. 1d). The melt is very homogeneous when analysed with an electron beam in raster mode (Table 2). Individual mineral grains occasionally show compositional zoning especially in runs at T ≤ 1,000°C: garnet may contain diffuse cores with variable Al/Cr ratios

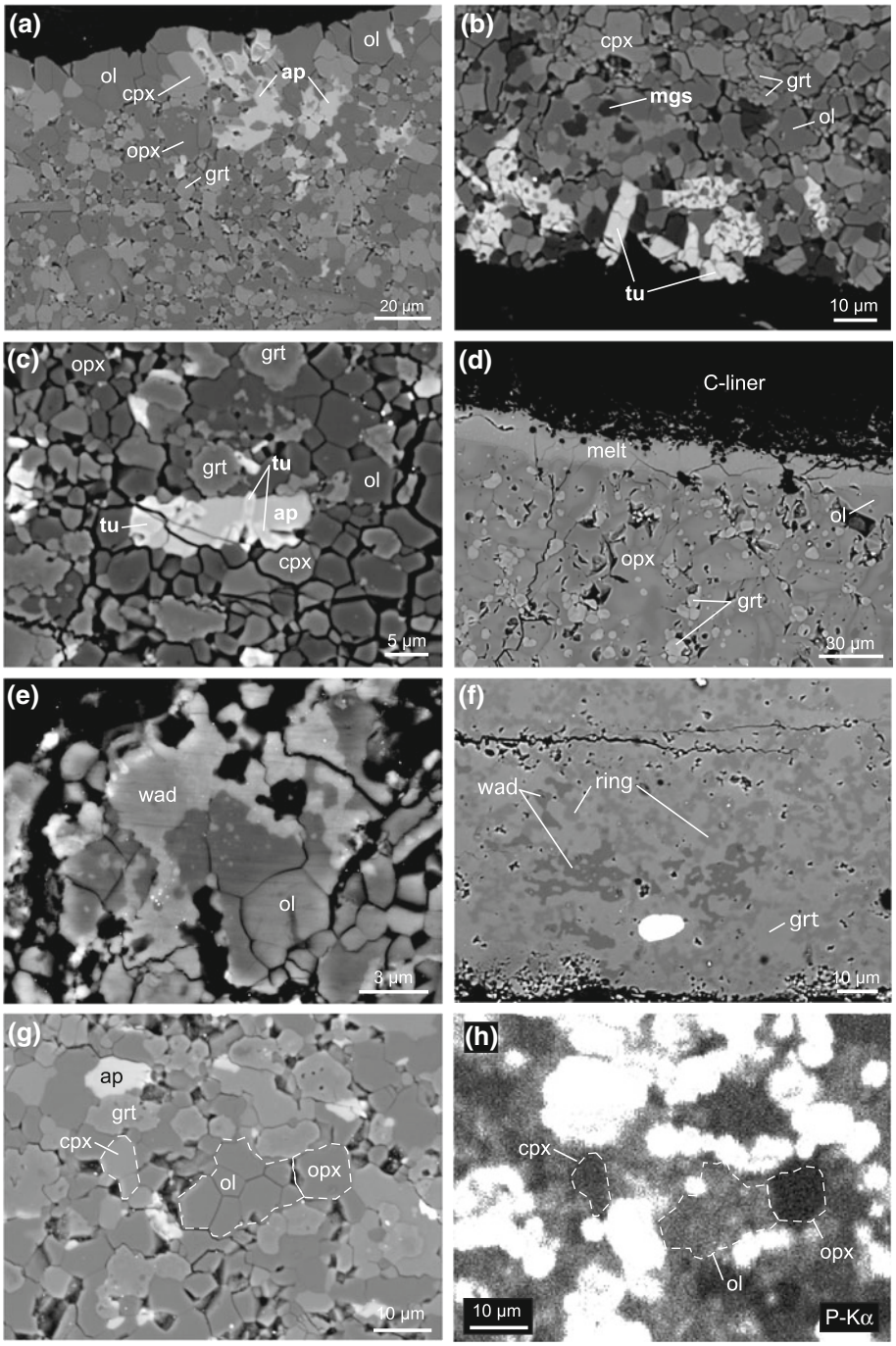

Fig. 1 Backscattered electron photomicrographs of experimental run products: **a** run MA52 at 7 GPa/1,000°C; **b** run B07-1 at 9 GPa/1,100°C; **c** run MA46 at 8.7 GPa/1,000°C; **d** run B06-11 at 6 GPa/1,500°C; **e** run B07-2 at 12.8 GPa/1,200°C; **f** run B08-5 at 19 GPa/1,200°C; **g** run MA31 at 4 GPa/1,000°C; **h** distribution of phosphorus in run MA31; mapped area corresponds to area shown in **g**; for better comparison between **g** and **h**, olivine, clinopyroxene and orthopyroxene are marked with stippled lines; for abbreviations, see Table 3

probably due to the sluggish diffusion of Al and Cr in the garnet structure and orthopyroxenes may show patchy Fe–Mg zoning with Fe-poor rims probably due to Fe-loss in the presence of melt (Fig. 1d). Cloudy phosphorus zoning in olivine may also be observed (Fig. 1h). In the Cl-bearing bulk compositions, severe Fe-loss with variable Fe contents and Fe–Mg zoning may even occur under subsolidus conditions (Fig. 1a) in experiments of long times (e.g. MA52 and MA55).

Phase relations

Bulk composition I crystallizes Mg_2SiO_4 + orthopyroxene + clinopyroxene + garnet ± apatite ± tuite in the PT range 6–15 GPa and 1,050–1,300°C. Apatite is stable in runs between 6 and 8 GPa to 1,100°C, and tuite was found between 8 and 15 GPa to 1,300°C. At 8 GPa/1,050°C, apatite and tuite coexist. Olivine is replaced by coexisting olivine + wadsleyite at 12.8 GPa (Fig. 1e). At 15 and 19 GPa, wadsleyite and coexisting wadsleyite and ringwoodite, respectively, are the stable Mg_2SiO_4 polymorphs (Fig. 1f). Quenched melt was found in two runs at 6 GPa/1,300°C coexisting with olivine + orthopyroxene + clinopyroxene + garnet and at 6 GPa/1,500°C coexisting with olivine + orthopyroxene + garnet (Fig. 2a). In bulk composition II, apatite is stable to 8.7 GPa at 1,000°C and coexists with olivine + orthopyroxene + clinopyroxene + garnet. Additional phases are calcic amphibole + phlogopite at 2.5 GPa and phlogopite at 4–5 GPa. At 8.7 GPa, apatite and tuite coexist (Fig. 1c). No potassic silicate phase was found between 7.0 and 8.7 GPa. Instead, tiny (≤1 μm) grains of K (Nb, Ta)O_3 are present, and X-ray mapping revealed diffuse potassium along grain boundaries of graphite close to the interface between experimental charge and graphite liner. The addition of extra 10% phlogopite to bulk composition II (bulk IIa) led to the formation of K-richterite coexisting with olivine + orthopyroxene + clinopyroxene + garnet + apatite at 7 GPa/800°C.

Phase compositions

Apatite and Tuite

Apatite and tuite always contain variable amounts of MgO, FeO, SrO, Na_2O and RE_2O_3 often reaching a wt% level (Table 2), with Na and REE showing a distinct positive correlation (Fig. 3a). Whereas MgO shows a strong increase with pressure from 0.7 wt% at 2.5 GPa to 3.1 wt% at 8.7 GPa, FeO contents only slightly increase from 0.4 to 1.1 wt% (Fig. 3b). The highest FeO + MgO values correspond to 9 mol% $(Mg, Fe)_5(PO_4)_3$ (OH). It is only in bulk composition III at 7 GPa/800°C that apatite shows unusually low concentrations of Mg and other minor elements. A possible reason is insufficient equilibration of these elements at the lowest temperatures attained in this study. None of the other minor elements shows a systematic correlation between concentration and pressure or temperature. The Cl content of apatite is between 0.4 and

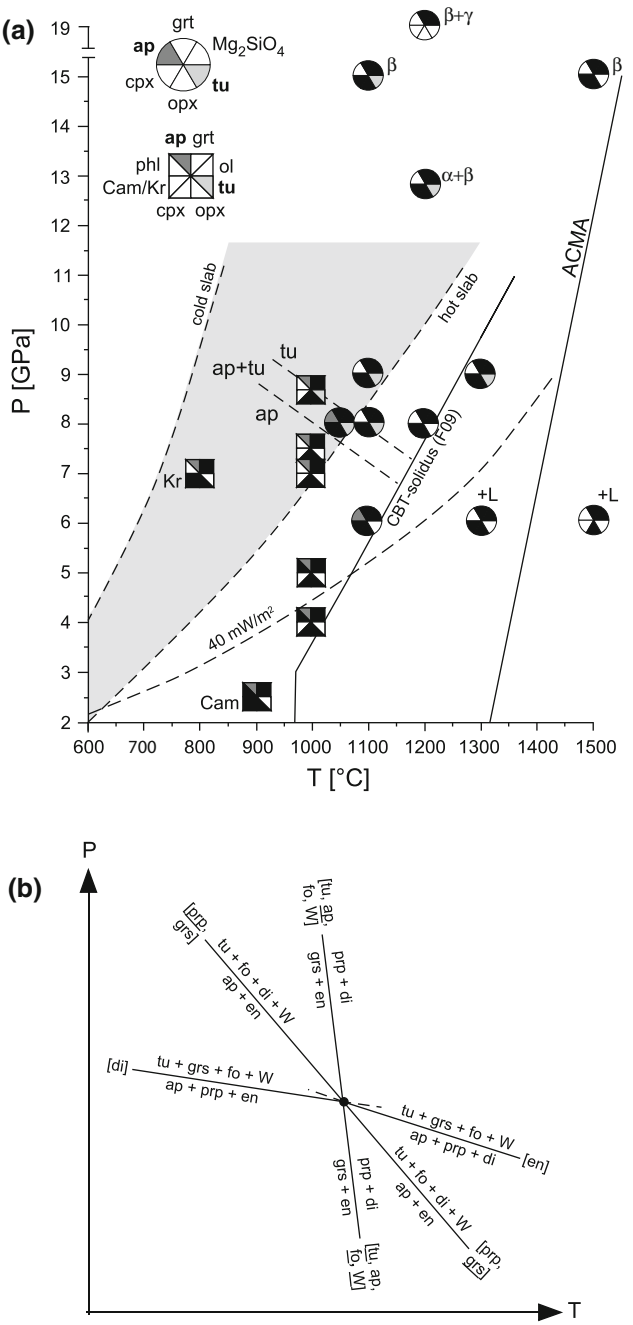

Fig. 2 **a** PT diagram summarizing experimental results obtained for bulk composition I (*round pie-symbols*), II and III (*square pie-symbols*); ACMA average current mantle adiabat for a surface potential temperature of 1,280°C; CBT-solidus (F09) solidus for CO_2–H_2O-bearing K-enriched pyrolite according to Foley et al. (2009); **b** schematic arrangement of possible tuite-forming reactions based on a negative slope of diopside- and enstatite-absent reactions (see text)

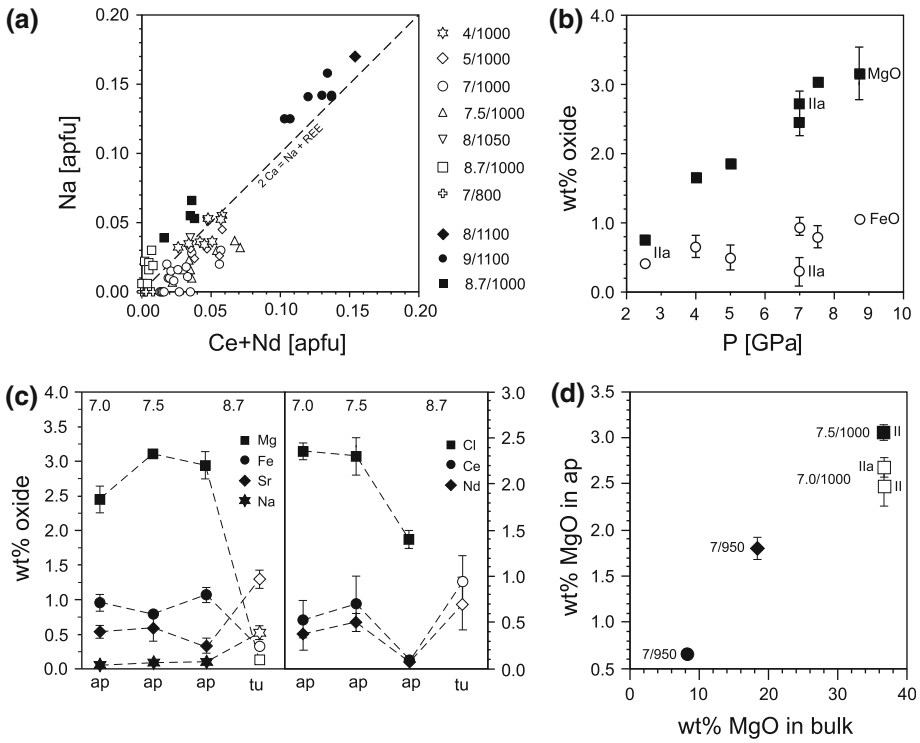

Fig. 3 **a** Na and REE content of apatite (*open symbols*) and tuite (*black symbols*); *numbers next to plot symbols* are pressure [GPa] and temperature [°C]; **b** averaged FeO and MgO contents of apatite from bulk compositions II and IIa; **c** minor element composition of apatite (*black symbols*) and coexisting apatite and tuite (*open symbols*) at 7–8.7 GPa/1,000°C; **d** relation between MgO in apatite and in the bulk; II and IIa: bulk compositions II and IIa; *black circle* and *diamond* are data from Konzett and Frost (2009)

2.4 wt% and thus significantly lower than the stoichiometric Cl content of 6.8 wt% of pure Cl-apatite. Possible reasons for this Cl-loss are discussed below. Tuite always shows significantly higher Sr and REE and lower Fe and Mg contents than apatite. This is true for experiments in which tuite is the only phosphate phase and also when apatite and tuite coexist (Fig. 3c; Table 2).

Hydrous silicates

Phlogopite shows little compositional variation between 2.5 and 5.0 GPa with Si = 2.89–2.97 apfu, K = 0.72–0.85 apfu and K/(K + Na) = 0.85–0.97. All phlogopites contain Cl in the range 0.23 ± 0.05 to 0.41 ± 0.05 wt% corresponding to $X_{Cl\text{-}phl}$ = 0.011–0.024. At 2.5 GPa/900°C, pargasitic calcic amphibole with Na (M4) = 0.12 apfu, Na (A) = 0.70 apfu, K/(K + Na) = 0.20 and Cl = 0.19 ± 0.05 wt% ($X_{Cl\text{-}amph}$ = 0.023) coexists with phlogopite. The major element composition of both phlogopite and calcic amphibole is in good agreement with experimental data by Fumagalli et al. (2009). In bulk composition III, K-richterite is the stable hydrous silicate at 7 GPa/800°C. Its composition is close to endmember $KNaCa(Mg, Fe)_5Si_8O_{22}(OH)_2$ with <0.1 wt% TiO_2 and Cr_2O_3 and an average Cl of 0.56 ± 0.07 wt% (n = 8) (Table 2).

Garnet

Garnets are pyrope-rich pyrope-almandine-grossular solid solutions typical for peridotites with minor amounts of Cr_2O_3, P_2O_5, Na_2O and TiO_2 (Table 2). P_2O_5 and Na_2O increase with increasing pressure from just above the detection limit at 2.5 GPa to 1.5–1.6 and 0.3–0.5 wt%, respectively, at P > 12.8 GPa (Figs. 4, 5). TiO_2 is present in concentrations of 0.1–0.4 wt% and shows little variation with pressure but an increase with temperature. A significant decrease in P, Na, Ti and X_{Mg} along with an increase in Cr can be observed at 6 GPa between 1,100 and 1,300°C and also at 8 GPa between 1,100 and 1,200°C accompanied by the disappearance of a phosphate phase.

Mg_2SiO_4 polymorphs

Under subsolidus conditions, olivine usually shows X_{Mg} values in the range 0.91–0.94. In the presence of melt (e.g. B06−11) or when long run durations were used (MA52), severe Fe-loss occurs in spite of the use of a graphite liner, resulting in X_{Mg} values of 0.96–1.00 (Table 2). Phosphorus contents in olivine range between 0.14 ± 0.03 and 0.23 ± 0.06 wt% P_2O_5 and do not show any significant correlation with pressure, temperature, X_{Mg} or grain size (Table 2). Run MA52 with the largest olivine single crystals or aggregates of up to 30 × 30 μm in diameter (Fig. 1a) yields 0.180 ± 0.040 (n = 15) wt% P_2O_5. Mapping of P_2O_5 concentrations of individual olivine grains in runs MA52 reveals variations in the range 0.10–0.22 wt%. In run B07-2, the olivine–wadsleyite loop is intersected. Based on Katsura and Ito (1989), X_{Mg} of the coexisting polymorphs at 1,200°C indicates a pressure of 12.8 GPa. Compared to P ≤ 9 GPa, phosphorus in both olivine and

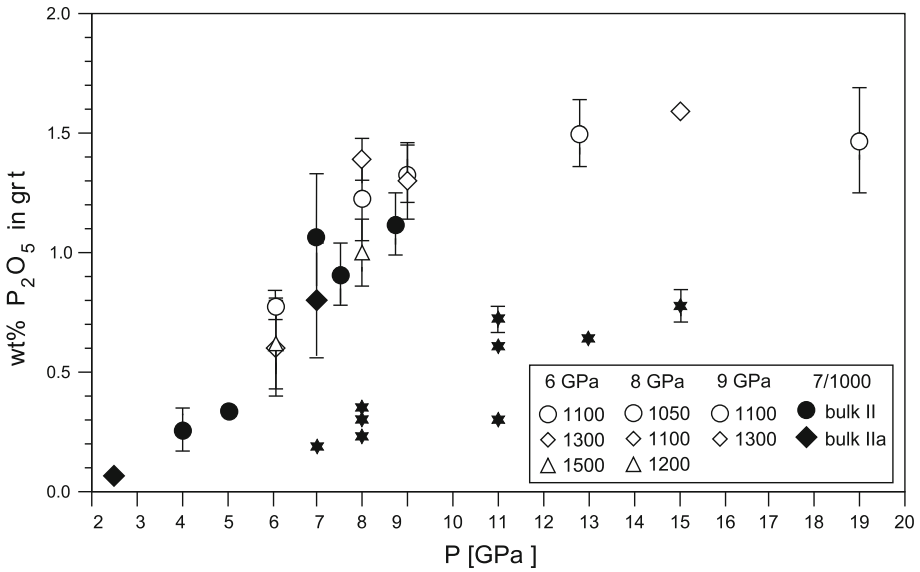

Fig. 4 Averaged phosphorus contents in garnet as a function of P and T; at 15 GPa, only results from run B06-16 are shown; *black stars* are data from garnet from a MORB-bulk shown for comparison (Konzett and Frost 2009)

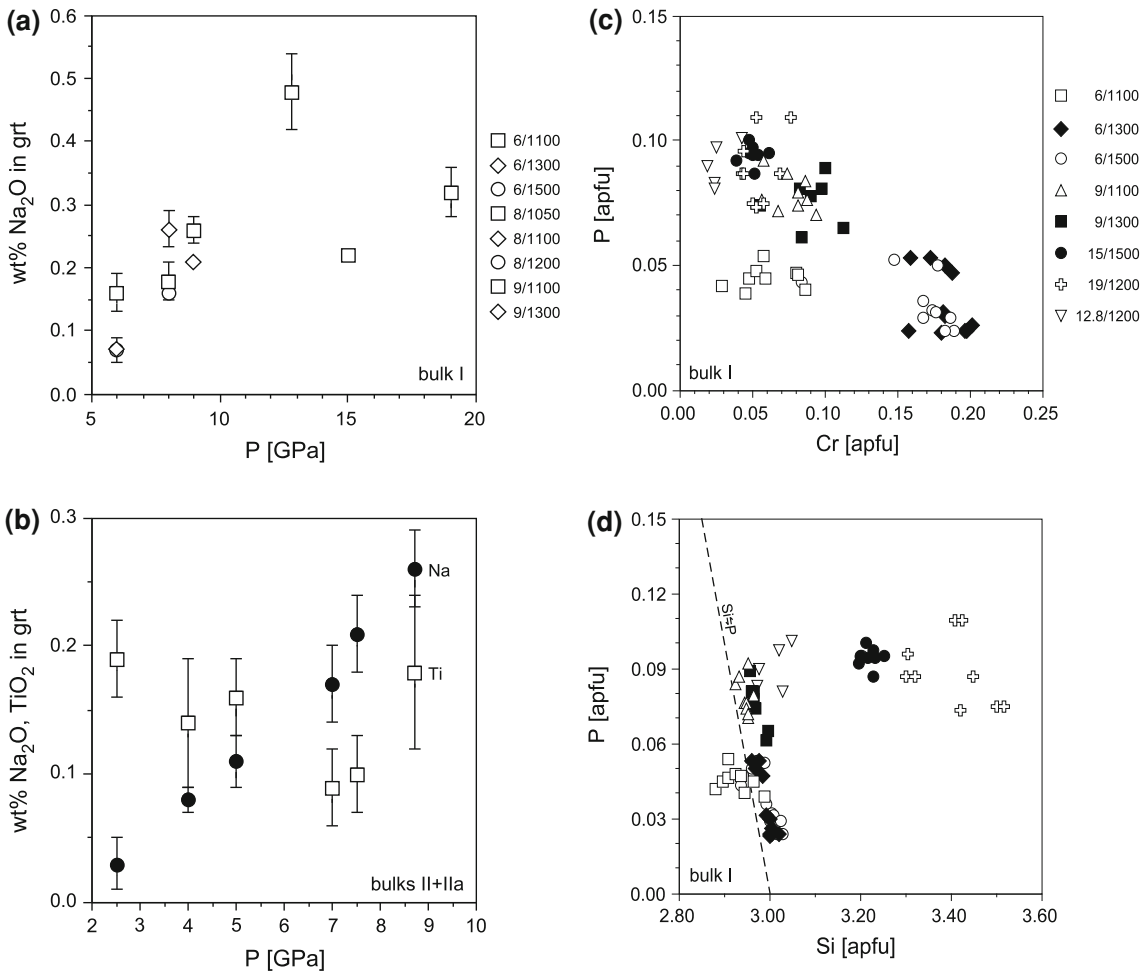

Fig. 5 a, b Averaged Na_2O and TiO_2 contents of garnets as a function of pressure and temperature; **c, d** P–Cr–Si systematics in garnets from bulk composition I; data scatter especially of the 6 GPa/1,100°C data is thought to be due to incomplete equilibration as a result of sluggish Cr diffusion

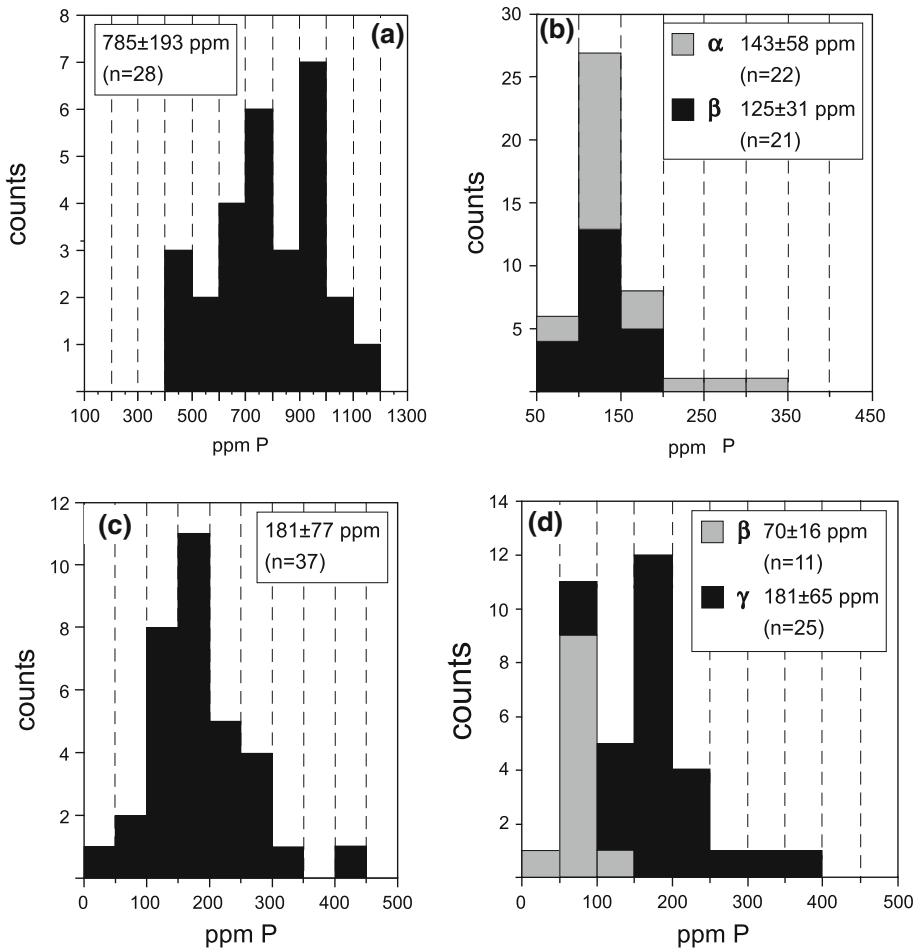

Fig. 6 Range of phosphorus concentrations in Mg_2SiO_4 polymorphs; **a** olivine in run MA52 at 7 GPa/1,000°C; **b** coexisting olivine (**a**) and wadsleyite (**b**) in run B07-2 at 12.8 GPa/1,200°C; **c** wadsleyite in run B06-16 at 15 GPa/1,500°C; **d** coexisting wadsleyite and ringwoodite (g) in run B08-5 at 19 GPa/1,200°C

wadsleyite buffered by tuite is significantly lower with 143 ± 58 ($n = 22$) ppm and 125 ± 31 ($n = 21$) ppm, respectively, showing an equal preference for the olivine and wadsleyite structures. Similarly, low concentrations of 181 ± 77 ($n = 37$) ppm are found in wadsleyite at 15 GPa/1,500°C in the absence of a phosphate phase. In run B08-5 conducted at 19 GPa/1,200°C, coexisting wadsleyite and ringwoodite with X_{Mg} of 0.935 and 0.897, respectively, are present. This is consistent with a pressure of ~17.5 GPa based on the wadsleyite–olivine loop deduced by Katsura and Ito (1989). Unlike coexisting olivine and wadsleyite, coexisting wadsleyite and ringwoodite show significantly different phosphorus concentrations of 70 ± 16 ($n = 11$) ppm and 181 ± 65 ($n = 25$) ppm, respectively (Fig. 6), indicating a preference of phosphorus for the ringwoodite structure.

Pyroxenes

Clinopyroxene are diopside-rich solid solutions with small amounts of jadeite, enstatite and Ca-Tschermaks pyroxene component. With the exception of a slight decrease in jadeite component with increasing pressure and temperature, there is little variation in the clinopyroxene composition. Averaged P_2O_5 contents are in the range of 352 ± 52 to 522 ± 86 ppm (Table 2). Orthopyroxene shows a decrease in Al with pressure constrained by coexisting garnet and an increase in Ca and Na with temperature, the former constrained by coexisting clinopyroxene. In the presence of melt, the Fe contents drop significantly and show a much stronger scatter compared to subsolidus conditions. The P_2O_5 contents of orthopyroxene range between 56 ± 24 ppm and 212 ± 44 ppm (Table 2).

Melt

Melts found in runs B06−11 and B06−13 in bulk composition I are carbonatitic due to oxidation of C from the graphite liner with SiO_2, CaO and MgO contents of 3.6–4.6 wt%, 23.5–25.2 wt% and 20.6–22.3 wt%, respectively, corresponding to Ca/(Ca + Mg) = 0.45–0.46. Both melts are strongly enriched in phosphorus with 7.6 and 8.1 wt% P_2O_5, respectively. In addition and not surprisingly, high concentrations of Sr, Ce and Nd were measured in the melt from run B06−11 (Table 2).

Discussion

The stability of apatite in peridotitic compared to MORB-type lithologies

This study shows that in a peridotite apatite is stable to at least 8.7 GPa at 1,000°C, which corresponds to a depth of ~260 km. This is ~1 GPa above the upper pressure stability limit of apatite in a MORB-type bulk composition (Konzett and Frost 2009). In addition, apatite and tuite coexist at 8.0 and 8.7 GPa in the peridotite bulk composition, whereas no indication for a significant pressure–temperature interval of coexisting apatite and tuite was found in a MORB-type bulk (cf. Konzett and Frost 2009). A possible explanation for the extended pressure stability of apatite in the peridotite is the stabilizing effect of MgO and FeO. Because of the high variance of the peridotite + Ca-phosphate assemblage, mineral and bulk compositions are interdependent, leading to much higher MgO in apatite from peridotites compared to that from MORB-type bulks (Fig. 3d). In a simplified system SiO_2 + MgO + CaO + Al_2O_3 + P_2O_5 + H_2O, in which the lherzolite + phosphate assemblage is represented by the phase components forsterite, enstatite, diopside, pyrope, grossular, apatite, tuite and H_2O-fluid, possible tuite-forming reactions are

$$2\,\text{apatite} + 3\,\text{enstatite} = 3\,\text{tuite} + \text{forsterite} + \text{diopside} + H_2O \quad (1)$$

$$4\,\text{apatite} + \text{pyrope} + \text{diopside} = 6\,\text{tuite} + \text{grossular} + 2\,\text{forsterite} + H_2O \quad (2)$$

$$6\,\text{apatite} + \text{pyrope} + 3\,\text{enstatite} = 9\,\text{tuite} + \text{grossular} + 3\,\text{forsterite} + H_2O \quad (3)$$

Based on the negative slope of the reaction grossular + 3 enstatite = pyrope + 3 diopside and experimental evidence for a negative slope of the tuite-forming reaction(s) (Fig. 2a), a possible arrangement in pressure and temperature of the reactions is shown in Fig. 2b. The stoichiometry of the apatite breakdown reaction cannot be unambiguously identified due to the absence of apatite breakdown products in addition to the phases present and the lack of significant compositional changes of garnet and pyroxene across the apatite–tuite breakdown pressure–temperature interval. In bulk composition II, increasing Ca and decreasing Mg in garnet between 7.5 and 8.7 GPa would be consistent with both reactions (2) and (3). The experiments of this study also show that apatite is stable to at least 1,100°C at 6 GPa and to 1,050–1,100°C at 8 GPa. The maximum temperature at which tuite was found is 1,300°C at 9 GPa. Within the spacing of experimental data points, there is no evidence for an extended stability of apatite or tuite coexisting with a melt. At 8 GPa for example, tuite disappears between 1,100 and 1,200°C, and at 1,200°C, the assemblage is olivine + orthopyroxene + clinopyroxene + garnet. In summary, the experimental data show that both apatite and tuite are stable in a wide range of subduction zone PT regimes and that apatite may also be present in cool lithospheric mantle to ~5–6 GPa (Fig. 2a). The absence of tuite from the experiment at 15 GPa/1,500°C further indicates that tuite is not stable in convecting asthenospheric mantle.

Phosphorus in peridotitic upper mantle phases and implications for phosphorus mobility in the upper mantle

The experiments of this study show that garnet has by far the highest phosphorus content of any solid upper mantle silicate phase. Phosphorus concentrations systematically increase with pressure from >0.1 wt% P_2O_5 at 2.5 GPa/900°C to 1.6 wt% P_2O_5 at 15 GPa/1,500°C (Fig. 4) and decrease with increasing temperature once the solidus is crossed due to preferential partitioning into coexisting melt. This increase is coupled to decreasing Si at P ≤ 12.8 GPa (Fig. 5d), confirming the extreme preference of phosphorus to substitute for $^{[4]}Si$ irrespective of the chemical system. The systematic increase in Na with pressure (Figs. 5a, b) indicates that the exchange $^{[8]}Na^{[4]}P^{[8]}M^{2+}{}_{-1}{}^{[4]}Si_{-1}$ is operative. Due to the low bulk Na content of peridotite, however, coupled Na–P incorporation into garnet can only account for a minor portion of the observed phosphorus. If R^{1+} cations are not available, phosphorus can still enter the garnet structure via $^{[6]}M^{2+[4]}P^{[6]}M^{3+}{}_{-1}{}^{[4]}Si_{-1}$ (Brunet et al. 2006). Whereas no correlation is obvious between Al and P, a negative correlation can be observed between P and Cr (Fig. 5c). This shows (1) that the berlinite substitution $^{[4]}Al^{3+[4]}P^{[4]}Si_{-2}$ is not operative and (2) that $^{[6]}M^{2+[4]}P^{[6]}Cr^{3+}{}_{-1}{}^{[4]}Si_{-1}$ with a minor contribution of $^{[8]}Na^{[4]}P^{[8]}M^{2+}{}_{-1}{}^{[4]}Si_{-1}$ is most likely to be responsible for phosphorus incorporation into the peridotitic garnets. Compared to MORB-type bulk compositions where $^{[8]}Na^{[4]}P^{[8]}M^{2+}{}_{-1}{}^{[4]}Si_{-1}$ is dominant (cf. Konzett and Frost 2009), phosphorus concentrations in peridotitic garnets are significantly higher across the entire PT range investigated (Fig. 4).

Mechanisms for phosphorus incorporation into the Mg_2SiO_4 polymorphs are difficult to deduce at the levels of P_2O_5 contents encountered in this study. All schemes proposed so far assume that phosphorus substitutes for tetrahedral Si with charge balance maintained by octahedral vacancies possibly coupled with the introduction of trivalent cations (Milman-Barris et al. 2008 and references therein). The variability in the phosphorus concentration of individual olivine grains observed in this study (cf. Figs. 1h, 6) is consistent with results from olivine

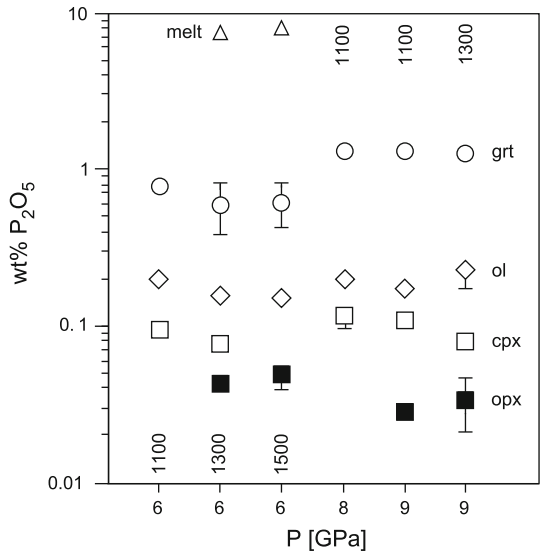

Fig. 7 Averaged phosphorus contents of coexisting peridotite phases from bulk composition I in the PT range 6–9 GPa and 1,100–1,500°C

crystallization experiments by Milman-Barris et al. (2008). These authors consider two possible mechanisms for local phosphorus enrichment in olivine, both of which result from rapid crystal growth in the presence of melt: (1) phosphorus enrichment in melt boundary layers adjacent to growing olivine, which may lead to elevated phosphorus contents in olivine due to equilibrium partitioning and (2) sluggish phosphorus diffusion in the melt away from the advancing crystal face, resulting in elevated phosphorus contents of olivine due to disequilibrium partitioning. In the present study, melt–crystal boundary layer effects can only play a significant role in the experiments at 1,300 and 1,500°C where quenched melt is present. At lower temperatures (e.g. MA52 or MA31), heterogeneous phosphorus distribution on a micrometre scale in the starting material combined with sluggish solid-state diffusion involving cations on several crystallographic sites is the likely reason for the observed phosphorus zoning in olivine.

Considering all averaged phosphorus concentrations, a consistent succession of the relative enrichment of phosphorus in the peridotitic phases can be observed with $P_{melt} \gg P_{grt} \gg P_{Mg2SiO4} > P_{cpx} > P_{opx}$ (Figs 1h, 7). Resulting values for $D_P^{mineral/melt}$ are between 0.08 for garnet and 0.006 for orthopyroxene (Table 4). This is consistent with phosphorus partitioning amongst spinel lherzolite phases measured by Brunet and Chazot (2001) albeit with a considerably lower absolute phosphorus concentration for the silicate melt reported by these authors. Bishop et al. (1978) found slightly higher phosphorus contents in clinopyroxene than in olivine in a suite of peridotite xenoliths from South African kimberlites with $P_{grt} > P_{cpx} > P_{ol} > P_{opx}$. The phosphorus contents of melt and coexisting clinopyroxene of this study are consistent with results on apatite solubility in carbonatitic melts at 3 GPa obtained by Baker and Wyllie (1982). The data from 6 GPa/1,300°C and 1,500°C combined with averaged garnet peridotite facies mineralogy (McDonough and Rudnick 1998) yield bulk phosphorus partition coefficients for mantle lherzolites of 0.018–0.024 (Table 4). These values are higher than those

Table 4 Phosphorus partition coefficients based on averaged P_2O_5 contents of mineral phases from high PT experiments compared to literature data

P [GPa]/T [°C]	$D^{grt/ol}$	$D^{grt/cpx}$	$D^{grt/opx}$	$D^{grt/melt}$	$D^{ol/melt}$	$D^{cpx/melt}$	$D^{opx/melt}$
6/1,100	3.9	8.0	–	–	–	–	–
6/1,300	3.9	7.8	13.6	0.08	0.02	0.01	0.006
6/1,500	4.1	–	12.7	0.08	0.02	–	0.006
8/1,100	6.6	10.9	–	–	–	–	–
9/1,100	7.8	12.1	40.3	–	–	–	–
9/1,300	5.7	16.1	38.2	–	–	–	–

Bulk partition coefficients and phosphorus storage capacity of mantle rocks

	ol	opx	cpx	grt	D	D (B&W)	$P_2O_5^{silicates}$	$P_2O_5^{apatite}$
Primitive mantle	57	16	14	13	0.0240	0.0041	0.30	0.71
Orogenic massifs	66	17	12	6	0.0202	0.0036	0.23	0.54
Off-craton lherz.	68	18	11	3	0.0182	0.0033	0.19	0.46
On-craton harzb.	83	15	–	2	0.0174	0.0029		

Modal amounts of peridotite phases according to McDonough & Rudnick (1998); D bulk partition coefficients for primitive mantle, orogenic massifs and off-craton lherzolites based on data from 6 GPa/1,300°C; value for on-craton harzburgite based on data from 6 GPa/1,500°C; D (B&W) D values by Baker & Wyllie (1992) $P_2O_5^{silicates}$ phosphate-saturated phosphorus storage capacity [wt% P_2O_5] of peridotite based on averaged P_2O_5 contents of grt, ol and cpx from run B07-11 and of opx from run B07-1; $P_2O_5^{apatite}$ modal amount of apatite [wt%] required to furnish P_2O_5 for the silicates

calculated by Baker and Wyllie (1992) based on their experimental data and phosphorus analyses of natural peridotite minerals due to the markedly higher phosphorus contents in olivine and garnet. Using averaged P_2O_5 concentrations of the peridotite silicates obtained in this study, the phosphorus storage capacity of a garnet–lherzolite at PT conditions close to the apatite ⇒ tuite reaction is ~0.2–0.3 wt% dependent on the modal proportion of phases (Table 4). This amount can be supplied by an equivalent of ~0.5–0.7 wt% apatite and is a minimum estimate because it does not take into consideration the potential presence of an additional fluid. It should be kept in mind that although garnet has by far the highest P_2O_5 concentrations of any solid peridotite phase, olivine is no less important as a potential phosphorus carrier due to its large modal amount in peridotites. This is true even for primitive mantle with the highest amount of garnet where olivine and garnet contribute to the bulk phosphorus partition coefficient in almost equal proportions (cf. Table 4). Because phosphorus contents in olivine show no discernable pressure dependence, it can be assumed that the high phosphorus storage capacity of olivine extends to pressures <3 GPa. In fact, Brunet and Chazot (2001) reported P_2O_5 contents of 0.07–0.15 wt% in olivine from an apatite-bearing spinel lherzolite, which is in good agreement with 0.16 ± 0.03 ($n = 7$) wt% P_2O_5 found at 4 GPa/1,000°C. Hence, both data from natural rocks and the experiments show that olivine alone is capable of storing the entire phosphorus budget of peridotitic mantle and that the formation of a phosphate phase cannot be expected unless phosphorus is added metasomatically.

The experiments show that in the presence of apatite peridotitic garnet and olivine accommodate ≥0.25 and ≥0.16 wt% P_2O_5, respectively, as the pressure increases to ≥4 GPa (Fig. 4; Table 2). These high values are not found in garnets or olivines from orogenic peridotites. Whereas this can be simply explained by the low bulk phosphorus contents, even apatite-bearing peridotites contain garnet and olivine, which are very poor in phosphorus. For example, olivine and coexisting garnet with apatite and magnesite inclusions equilibrated at 850°C and 4.1 GPa in peridotites from the Bohemian Massif, Czech Republic, both contain <0.05 wt% P_2O_5 (Vrána 2009). This discrepancy indicates that substantial compositional changes of the peridotite phases take place during slow exhumation of orogenic peridotites similar to those inferred for MORB-type eclogite assemblages (Hermann and Spandler 2007; Konzett and Frost 2009).

Apatite associated with calcite/dolomite ± clinopyroxene ± phlogopite is often observed in peridotitic mantle xenoliths and taken as indication for the former (transient) presence of a phosphorus-rich carbonatitic melt (e.g. Green and Wallace 1988; Yaxley et al. 1991; Hauri et al. 1993; Coltorti et al. 1999; O'Reilly and Griffin 2000). Due to their extremely low viscosity (Dobson et al. 1996), carbonatitic melts are thought to migrate pervasively in small amounts along grain boundaries with a strong tendency of dispersing instead of pooling (Hammouda and Laporte 2000). This style of migration inhibits large-scale melt segregation and promotes solid/melt element exchange, thus making carbonatites eminently suitable agents for mantle metasomatism. The results from this study and the rare data for phosphorus in silicates from natural peridotites both indicate that even in shallow upper mantle, a small amount of phosphorus-rich carbonatitic melt would quickly get stripped of its phosphorus when travelling through previously unmetasomatized garnet + olivine-bearing mantle. Hence, transport of phosphorus via carbonatitic melts is only possible (1) if garnet and olivine are already saturated in phosphorus as a result of an earlier episode of carbonatite impregnation, (2) if the fluid/melt-rock ratio is sufficiently high to exhaust the storage capacity of garnet and olivine or (3) through a transport mechanism that is fast enough to prevent equilibration between melt and peridotitic country rocks. Extremely fast magma ascent at a speed on the order of metres per second caused by high-speed dike propagation (Sparks et al. 2006; Wilson and Head 2007; Peslier et al. 2008) thus must play an important role in the preservation of the high bulk phosphorus contents of up to several wt% P_2O_5 typical of kimberlites and orangeites (Le Roex et al. 2003; Mitchell 1995). The same is true for certain P_2O_5-rich magnesiocarbonatites and leucitites (Dalton and Presnall 1998; Bailey 1989; Humphreys et al. 2010).

Potassium and chlorine transport in peridotitic mantle—the role of apatite and hydrous silicates

In recent years, an increasing number of reports have been published on K–Cl-P-LILE-rich hypersaline brines and carbonatitic fluids or melts and associated K–Cl-rich solid inclusions in diamonds (Tomlinson et al. 2005; Schrauder and Navon 1994; Klein-BenDavid et al. 2006; Wirth et al. 2009; Izraeli et al. 2001, 2004). These exotic fluids/melts show that at least on a local scale, substantial amounts of Cl must be present in the subcontinental mantle at depths >150 km in spite of the very high recycling efficiency assumed for Cl in subduction zones (e.g. Straub and Layne 2003). Because K–Cl-carbonatitic fluids/melts are not permanently present under subduction zone PT conditions and also in cool lithospheric mantle at least to pressures ≤5 GPa (Fig. 2a), solid Cl carriers must play an important role in the long-term storage of Cl in the mantle and may become the source of Cl-rich fluids/melts during renewed heating. The present study indicates that apatite is a potential Cl carrier to a depth of ≤150–180 km under

Table 5 Chlorine partition coefficients for coexisting apatite, phlogopite and amphibole based on their averaged Cl contents

Run no.	JKI-98	MA31	MA21	MA55
P [GPa]/T [°C]	2.5/900	4.0/1,000	5.0/1,000	7.0/800
wt% Cl in ap (*n**)	0.99 ± 0.02 (5)	0.65 ± 0.07 (8)	1.35 ± 0.10 (5)	0.90 ± 0.13 (8)
wt% Cl in phl (*n*) (*n*)	0.40 ± 0.08 (4)	0.23 ± 0.05 (9)	0.41 ± 0.05 (7)	–
wt% Cl in Cam (*n*)	0.19 ± 0.05 (4)	–	–	–
wt% Cl in Kr (*n*)	–	–	–	0.56 ± 0.07 (8)
$(X_{Cl}/X_{OH})^{ap}$	0.162 ± 0.004	0.101 ± 0.011	0.243 ± 0.026	0.146 ± 0.025
$(X_{Cl}/X_{OH})^{phl}$	0.025 ± 0.005	0.014 ± 0.003	0.025 ± 0.004	–
$(X_{Cl}/X_{OH})^{Cam}$	0.024 ± 0.006	–	–	–
$(X_{Cl}/X_{OH})^{Kr}$	–	–	–	0.073 ± 0.009
X_{Fe}^{phl}	0.057 ± 0.003	0.057 ± 0.009	0.040 ± 0.020	–
X_{Fe}^{Cam}	0.074 ± 0.002	–	–	–
X_{Fe}^{Kr}	–	–	–	0.114 ± 0.014
$K_{D,Cl}^{ap\text{-}phl}$**	6.48	7.21	9.72	–
$K_{D,Cl}^{ap\text{-}Cam}$	6.75	–	–	–
$K_{D,Cl}^{ap\text{-}Kr}$	–	–	–	2.00

* number of analyses,
** $K_D = (X_{Cl}/X_{OH})^{ap}/(X_{Cl}/X_{OH})^{hydrous\ silicate}$

conditions of a 40 mW/m^2 geotherm. At greater depths/higher temperatures, the apatite–peridotite solidus is intersected in a carbon-saturated mantle (Fig. 2a), resulting in the disappearance of apatite and the formation of P–Cl-rich carbonatitic melts/fluids (e.g. Baker and Wyllie 1992). If present in modal amounts exceeding ~1% (cf. Table 4), apatite may reach its upper pressure stability limit in subduction zones at depths between ~250 and 300 km dependent upon the thermal regime.

Hydrous silicates capable of storing Cl are stable to at least 600 km depth in the mantle wedge above subduction zones. The succession of phases is calcic amphibole (≤3 GPa) → phlogopite (≤6.5 GPa) → K-richterite (≤15 GPa) → phase X (≤20 GPa) (Konzett and Fei 2000). The very small database on Cl in hydrous mantle silicates shows that Cl contents of phlogopites and calcic amphiboles are almost always <0.1 wt% and very rarely exceed 0.5 wt%. (Zanetti et al. 1996; Naemura et al. 2009; Matson et al. 1986; Smith et al. 1981; Zaccharini and Stumpfl 2004; Hervig and Smith 1981; Peng et al. 1995; Dawson 2002; Wartho and Kelley 2003). Cl contents of apatite by comparison are usually at least one order of magnitude higher and may reach ≥5 wt% (Bonatti et al. 1986; Woodland et al. 1996). This study shows that in peridotitic bulk compositions apatite can coexist with both phlogopite and K-richterite and that significant amounts of Cl are present in both silicate phases. In the PT range 2.5–5 GPa/900–1,000°C, $K_{D,Cl}^{ap-phl}$ values (cf. Zhu and Sverjensky 1992) are between 6.5 and 9.7 (Table 5). Although the Cl concentrations in apatite and phlogopite in the 4 and 5 GPa runs are different probably due to variable Cl-loss to a fluid, the K_D-values are similar, indicating that Cl exchange equilibrium was at least approached. At 7 GPa/800°C, coexisting apatite and K-richterite yield $K_{D,Cl}^{ap\text{-}Kr} = 2.0$ with 0.56 ± 0.07 and 0.90 ± 0.13 wt% Cl in K-richterite and apatite, respectively. This shows that K-richterite is a suitable Cl carrier and potentially important for the crust-to-mantle transfer of Cl in subduction zone peridotites in a depth range of ~250 to 450 km.

Whereas phlogopite is stable at 4 and 5 GPa in bulk composition II, no solid potassic silicate was found at 7.0 and 7.5 GPa. By comparison, in Cl-free peridotites containing almost identical amounts of potassium and water, potassic silicates are continuously stable to ≥12 GPa (Konzett and Ulmer 1999; Konzett and Fei 2000). This indicates that Cl strongly raises the solubility of potassium in hydrous fluids[1] at P ≥ 7 GPa. Hence, such a fluid encountering an assemblage phlogopite/K-richterite + Cl-rich apatite may become Cl-enriched by preferential partitioning of Cl into the fluid. Given high enough pressures, the Cl-enrichment of the fluid strongly raises its potassium solubility and may trigger breakdown of phlogopite/K-richterite, thereby generating small amounts of fluids extremely rich in K, Cl and other incompatible elements. Evolving in a closed system, e.g. when trapped in a diamond, such a fluid would have the potential to crystallize unusual phases such as KCl or Cl-rich hypersilicic mica in addition to apatite and carbonates as observed in diamond micro-inclusions (e.g. Klein-BenDavid et al. 2006; Wirth et al. 2009).

Acknowledgments We would like to thank Hubert Schulze from BGI for the skilful preparation of experimental charges. Constructive and thoughtful reviews by Odet Navon and Alberto Patiño Douce helped to improve the manuscript and are gratefully acknowledged.

[1] The term 'fluid' is used in this context to denote any continuum between a solute-rich COH-fluid and a hydrous carbonatitic melt.

References

Armstrong JT (1995) CITZAF: a package of correction programs for the quantitative electron microbeam X-ray-analysis of thick polished materials, thin films, and particles. Microbeam Anal 4:177–200

Bailey DK (1989) Carbonate melt from the mantle in the volcanoes of south-east Zambia. Nature 338:415–418

Baker MB, Wyllie PJ (1992) High-pressure apatite solubility in carbonate-rich liquids: implications for mantle metasomatism. Geochim Cosmochim Acta 56:3409–3422

Bauer M, Klee WE (1993) The monoclinic-hexagonal phase transition in chlorapatite. Eur J Mineral 5:307–316

Bishop FC, Smith JV, Dawson JB (1978) Na, K and Ti in garnet, pyroxene and olivine from peridotite and eclogite xenoliths from African kimberlites. Lithos 11:155–173

Bonatti E, Ottonello G, Hamlyn PR (1986) Peridotites from the island of Zabargad (St. John), Red Sea: petrology and geochemistry. J Geophys Res 91(B1):599–631

Boyce JW, Liu Y, Rossman GR, Guan Y, Eiler JM, Stolper EM, Taylor LA (2010) Lunar apatite with terrestrial volatile abundances. Nature 466:466–470

Bromiley DW, Kohn SC (2007) Comparisons between fluoride and hydroxide incorporation into nominally fluorine-free mantle minerals. Geochim Cosmochim Acta 71:A124

Brunet F, Chazot G (2001) Partitioning of phosphorus between olivine, clinopyroxene and silicate glass in a spinel lherzolite xenolith from Yemen. Chem Geol 176:51–72

Brunet F, Bonneau V, Irifune T (2006) Complete solid-solution between $Na_3Al_2(PO_4)_3$ and $Mg_3Al_2(SiO_4)_3$ garnets at high pressure. Am Min 91:211–215

Coltorti M, Bonadiman C, Hinton RW, Siena F, Upton BGJ (1999) Carbonatite metasomatism of the oceanic upper mantle: evidence from clinopyroxenes and glasses in ultramafic xenoliths of Grand Comore, Indian Ocean. J Petrol 40:133–165

Dalton JA, Presnall DC (1998) Carbonatite melts along the solidus of model lherzolite in the system CaO-MgO-Al_2O_3-SiO_2-CO_2 from 3 to 7 GPa. Contrib Mineral Petrol 131:123–135

Dawson JB (2002) Metasomatism and partial melting in upper-mantle peridotite xenoliths from the Lashaine Volcano, Northern Tanzania. J Petrol 43:1749–1777

Dobson DP, Jones AP, Rabe R, Sekine T, Kurita K, Taniguchi T, Kondo T, Kato T, Shimomura O, Urakawa S (1996) In situ measurement of viscosity and density of carbonate melts at high pressure. Earth Planet Sci Lett 143:207–215

Exley RA, Smith JV (1982) The role of apatite in mantle enrichment processes and in the petrogenesis of some alkali basalt suites. Geochim Cosmochim Acta 46:1375–1384

Foley S (1992) Vein-plus-wall-rock melting mechanisms in the lithosphere and the origin of potassic alkaline magmas Lithos 28:435–453

Foley SF, Yaxley GM, Rosenthal A, Buhre S, Kiseeva ES, Rapp RP, Jacob DE (2009) The composition of near-solidus melts of peridotite in the presence of CO_2 and H_2O between 40 and 60 kbar. Lithos 112S:274–283

Fumagalli P, Zanchetta S, Poli S (2009) Alkali in phlogopite and amphibole and their effects on phase relations in metasomatized peridotites: a high-pressure study. Contrib Mineral Petrol 158:723–737

Green DH, Wallace ME (1988) Mantle metasomatism by ephemeral carbonatite melts. Nature 336:459–462

Greshake A, Fritz J (2009) Discovery of ringwoodite, wadsleyite, and in g-Ca_3 $(PO_4)_2$ in Chassigny: constraints on shock conditions. 40th lunar and planetary science conference, abstract 1586

Guthrie GD, Veblen DR, Navon O, Rossman GR (1991) Submicrometer fluid inclusions in turbid-diamond coats. Earth Planet Sci Lett 105:1–12

Hammouda T, Laporte D (2000) Ultrafast mantle impregnation by carbonatite melts. Geology 28:283–285

Hauri EH, Shimizu N, Dieu JJ, Hart SR (1993) Evidence for hotspot-related carbonatite metasomatism in the oceanic upper mantle. Nature 365:221–227

Hermann J, Spandler JC (2007) Sediment melts at sub-arc depth: an experimental study. J Petrol 49:717–740

Hervig RL, Smith JV (1981) Dolomite-apatite inclusion in chrome-diopside crystal, Bellsbank kimberlite, South Africa. Am Min 66:346–349

Humphreys ER, Bailey K, Hawkesworth CJ, Wall F, Najorka J, Rankin AH (2010) Aragonite in olivine from Calatrava, Spain—evidence for mantle carbonatite melts from greater than 100 km depth. Geology 38:911–914

Ionov DA, O'Reilly SY, Genshaft YS, Kopylova MG (1996) Carbonate-bearing mantle peridotite xenoliths from Spitsbergen: phase relationships, mineral compositions and trace-element residence. Contrib Mineral Petrol 125:375–392

Ionov DA, Hofmann AW, Merlet C, Gurenko AA, Hellebrand E, Montagnac G, Gillet P, Prikhodko VS (2006) Discovery of whitlockite in mantle xenoliths: Inferences for water- and halogen-poor fluids and trace element residence in the terrestrial upper mantle. Earth Planet Sci Lett 244:201–217

Izraeli ES, Harris JW, Navon O (2001) Brine inclusions in diamonds: a new upper mantle fluid. Earth Planet Sci Lett 187:323–332

Izraeli ES, Harris JW, Navon O (2004) Fluid and mineral inclusions in cloudy diamonds from Koffiefontein, South Africa. Geochim Cosmochim Acta 68:2561–2575

Katsura T, Ito E (1989) The system Mg_2SiO_4-Fe_2SiO_4 at high pressures and temperatures: precise determination of the stabilities of olivine, modified spinel, and spinel. J Geophys Res 94:15663–15670

Klein EM (2004) Geochemistry of the igneous oceanic crust. In: Rudnick RL (ed) The crust; Holland HD, Turekian KK (eds) Treatise on geochemistry, vol 3, Elsevier-Pergamon, Oxford, pp 433–465

Klein-BenDavid O, Wirth R, Navon O (2006) TEM imaging and analysis of microinclusions in diamonds: a close look at diamond-growing fluids. Am Min 91:353–365

Kolker A (1982) Mineralogy and geochemistry of Fe-Ti oxide and apatite (nelsonite) deposits and evaluation of the liquid immiscibility hypothesis. Econ Geol 77:1146–1158

Konzett J, Fei Y (2000) Transport and storage of potassium in the Earth's upper mantle and transition zone: an experimental study to 23 GPa in simplified and natural bulk compositions. J Petrol 41:583–603

Konzett J, Frost DJ (2009) The high P-T stability of hydroxyl-apatite in natural and simplified MORB–an experimental study to 15 GPa with implications for transport and storage of phosphorus and halogens in subduction zones. J Petrol 50:2043–2062

Konzett J, Ulmer P (1999) The stability of hydrous potassic phases in lherzolitic mantle–an experimental study to 9.5 GPa in simplified and natural bulk compositions. J Petrol 40:629–652

Konzett J, Frost DJ, Proyer A, Ulmer P (2008) The Ca-Eskola component in eclogitic clinopyroxene as a function of pressure, temperature and bulk composition: an experimental study to 15 GPa with possible implications for the formation of oriented SiO_2-inclusions in omphacite. Contrib Mineral Petrol 155:215–228

Kullerud K (1995) Chlorine, titanium and barium-rich biotites: factors controlling biotite composition and the implications for garnet-biotite geothermometry. Contrib Mineral Petrol 120:42–59

Lang AR, Walmsley JC (1983) Apatite inclusions in natural diamond coat. Phys Chem Miner 9:6–8

Le Roex AP, Bell DR, Davis P (2003) Petrogenesis of group I kimberlites from Kimberley, South Africa: evidence from bulk-rock geochemistry. J Petrol 44:2261–2286

Leshin L (2000) Insights into martian water reservoirs from analyses of martian meteorite QUE94201. Geophys Res Lett 14:2017–2020

Matson DW, Muenow DW, Garcia MO (1986) Volatile contents of phlogopite micas from South African kimberlite. Contrib Mineral Petrol 93:399–408

Matsumoto T, Honda M, McDougall I, Yatsevich I, O'Reilly SY (1997) Plume-like neon in a metasomatic apatite from the Australian lithospheric mantle. Nature 388:162–164

McCubbin FM, Steele A, Hauri E, Nekvasil H (2010) Quantitative SIMS analysis of OH in lunar apatite: implications for water in the lunar interior. Goldschmidt conference abstracts 2010, A687

McDonough WF (1990) Constraints on the composition of the continental lithospheric mantle. Earth Planet Sci Lett 101:1–18

McDonough WF, Rudnick RL (1998) Mineralogy and composition of the upper mantle. In: Hemley RJ (ed) Ultrahigh-pressure mineralogy, vol 37; Ribbe PH (ed) Reviews in mineralogy. Mineralogical Society of America, Washington DC, pp 139–164

McDonough WF, Sun SS (1995) Composition of the Earth. Chem Geol 120:223–253

Médard E, McCammon CA, Barr JA, Grove TL (2008) Oxygen fugacity, temperature reproducibility, and H_2O contents of nominally anhydrous piston-cylinder experiments using graphite capsules. Am Min 93:1838–1844

Milman-Barris MS, Beckett JR, Baker MB, Hofmann AE, Morgan Z, Crowley MR, Vielzeuf D, Stolper E (2008) Zoning of phosphorus in igneous olivine. Contrib Mineral Petrol 155:739–765

Mitchell RH (1995) Geochemistry of Orangeites. In: Kimberlites, Orangeites, and related rocks. Plenum Press, pp 249–301

Morishita T, Arai S, Tamura A (2003) Petrology of an apatite-rich layer in the Finero phlogopite-peridotite, Italian Western Alps; implications for evolution of a metasomatic agent. Lithos 69:37–49

Murayama JK, Nakai S, Kato M, Kumazawa M (1986) A dense polymorph of $Ca_3(PO_4)_2$: a high pressure phase of apatite decomposition and its geochemical significance. Phys Earth Planet Int 44:293–303

Naemura K, Hirajima T, Svojtka M (2009) The pressure-temperature path and the origin of phlogopite in spinel-garnet peridotites from the Blansky Les Massif of the Moldnaubian Zone, Czech Republic. J Petrol 50:1795–1827

O'Reilly SY, Griffin WL (1988) Mantle metasomatism beneath western Victoria, Australia: I. Metasomatic processes in Cr-diopside lherzolites. Geochim Cosmochim Acta 52:433–447

O'Reilly SY, Griffin WL (2000) Apatite in the mantle: implications for metasomatic processes and high heat production in Phanerozoic mantle. Lithos 53:217–232

O'Reilly SY, Griffin WL, Ryan CG (1991) Residence of trace elements in metasomatized spinel lherzolite xenoliths: a proton microprobe study. Contrib Mineral Petrol 109:98–113

Oberti R, Ungaretti L, Cannillo E, Hawthorne FC (1993) The mechanism of Cl incorporation into amphibole. Am Mineral 78:746–752

Ozawa S, Ohtani E, Suzuki A, Miyahara M, Terada K, Kimura M (2007) Shock metamorphism of L6 chondrites Sahara 98222 and Yamato 74445: the P-T conditions and the shock age. American Geophysical Union Fall Meeting, abstract #MR43B-1234

Palme H, O'Neill HStC (2004) Cosmochemical estimates of mantle composition. In: Carlson RW (ed) The mantle and core, vol 2. Holland HD, Turekian KK (eds) Treatise on geochemistry. Elsevier-Pergamon, Oxford, pp 1–39

Patiño Douce AE, Roden M (2006) Apatite as a probe of halogen and water fugacities in the terrestrial planets. Geochim Cosmochim Acta 70:3173–3196

Pearson DG, Canil D, Shirey SB (2004) Mantle samples included in volcanic rocks: xenoliths and Diamonds. In: Holland HD, Turekian KK (eds) Treatise on geochemistry, vol 3. Elsevier, Amsterdam, pp 171–275

Peng G, Lewis J, Lipin B, McGee J, Bao P, Wang X (1995) Inclusions of phlogopite and phlogopite hydrates in chromite from the Hongguleleng ophiolite in Xinjiang, northwest China. Am Mineral 80:1307–1316

Peslier AH, Woodland AB, Wolff JA (2008) Fast kimberlite ascent rates estimated from hydrogen diffusion profiles in xenolithic mantle olivines from Southern Africa. Geochim Cosmochim Acta 72:2711–2722

Rosenbaum JM, Wilson M, Condliffe E (1997) Partial melts of subducted phosphatic sediments in the mantle. Geology 25:77–80

Rudnick RL, Gao S (2003) Composition of the continental crust. In: Rudnick RL (ed) The Crust, vol 3. Holland HD, Turekian KK (eds) Treatise on geochemistry, Elsevier-Pergamon, Oxford, pp 1–64

Rudnick RL, McDonough WF, Chappell BW (1993) Carbonatite metasomatism in the northern Tanzanian mantle: petrographic and geochemical characteristics. Earth Planet Sci Lett 114:463–475

Schrauder M, Navon O (1994) Hydrous and carbonatitic mantle fluids in fibrous diamonds from Jwaneng, Botswana. Geochim Cosmochim Acta 58:761–771

Smith JV, Delaney JS, Hervig RL, Dawson JB (1981) Storage of F and Cl in the upper mantle: geochemical implications. Lithos 14:133–147

Sparks RSJ, Baker L, Brown RJ, Field M, Schumacher J, Stripp G, Walters A (2006) Dynamical constraints on kimberlite volcanism. J Volcanol Geotherm Res 155:18–48

Straub SM, Layne GD (2003) The systematics of chlorine, fluorine, and water in Izu arc front volcanic rocks: implications for volatile recycling in subduction zones. Geochim Cosmochim Acta 67:4179–4203

Sugiyama K, Tokonami M (1987) Structure and crystal chemistry of a dense polymorph of tricalcium phosphate $Ca_3(PO_4)_2$: a host to accommodate large lithophile elements in the Earth's mantle. Phys Chem Min 15:125–130

Thompson RN (1975) Is upper mantle phosphorus contained in sodic garnet? Earth Planet Sci Lett 26:417–424

Titkov SV, Gorshov AI, Zudin NG, Ryabchikov ID, Magazina LO, Sivtsov AV (2006) Microinclusions in dark grey diamond crystals of octahedral habit from Yakutian kimberlites. Geochem Int 44:1121–1128

Tomlinson E, De Schrijver I, De Corte K, Jones AP, Moens L, Vanhaecke F (2005) Trace element compositions of submicroscopic inclusions in coated diamond: a tool for understanding diamond petrogenesis. Geochim Cosmochim Acta 69:4719–4732

Volvinger M, Robert JL, Vielzeuf D, Neiva AMR (1985) Structural control of the chlorine content of OH-bearing silicatesa (micas and amphiboles). Geochim Cosmochim Acta 49:37–48

Vrána S (2009) Mineral inclusions in pyrope from garnet peridotites, Kolín area, central Czech Republic. J Geosci 53:17–30

Wartho J-A, Kelley SP (2003) 40Ar/39Ar ages in mantle xenolith phlogopites: determining the ages of multiple lithospheric mantle events and diatreme ascent rates in southern Africa and Malaita, Solomon Islands. Geol Soc Lond Spec Publ 220:231–248

Wass SY, Henderson P, Elliott CJ (1980) Chemical heterogeneity and metasomatism in the upper mantle: evidence from rare earth and

other elements in apatite-rich xenoliths in basaltic rocks from eastern Australia. Philos T R Soc Lond A A297:333–346

Wilson L, Head JW (2007) An integrated model of kimberlite ascent and eruption. Nature 447:53–57

Wirth R, Kaminsky F, Matsyuk S, Schreiber A (2009) Unusual micro- and nano-inclusions in diamonds from the Juina Area, Brazil. Earth Planet Sci Lett 286:292–303

Woodland AB, Kornprobst J, McPherson E, Bodinier J-L, Menzies MA (1996) Metasomatic interactions in the lithospheric mantle: petrologic evidence from the Lherz massif, French Pyrenees. Chem Geol 134:83–112

Workman RK, Hart SR (2005) Major and trace element composition of the depleted MORB mantle (DMM). Earth Planet Sci Lett 231:53–72

Xie X, Minitti ME, Chen M, Mao HK, Wang D, Shu J, Fei Y (2003) Tuite, γ-$Ca_3(PO_4)_2$: a new mineral from the Suizhou L6 chondrite. Eur J Mineral 15:1001–1005

Yaxley GM, Green DH, Kamenetsky V (1991) Evidence for carbonatite metasomatism in spinel peridotite xenoliths from western Victoria, Australia. Earth Planet Sci Lett 107:305–317

Zaccharini F, Stumpfl EF (2004) Zirconolite and Zr-Th-U minerals in chromitites of the Finero Complex, Western Alps, Italy: evidence for carbonatite-type metasomatism in a subcontinental mantle plume. Can Min 42:1825–1845

Zanetti A, Vannucci R, Botazzi P, Oberti R, Ottolini L (1996) Infiltration metasomatism at Lherz as monitored by systematic ion-microprobe investigations close to a hornblendite vein. Chem Geol 134:113–133

Zanetti A, Mazzucchelli G, Rivalenti G, Vannucci R (1999) The Finero phlogopite-peridotite massif: an example of subduction-related metasomatism. Contrib Mineral Petrol 134:107–122

Zhang W, Shao J, Xu X, Wang R, Chen L (2007) Mantle metasomatism by P- and F-rich melt/fluids: evidence from phosphate glass in spinel lherzolite xenolith in Keluo, Heilongjiang Province. Chin Sci Bull 52:1827–1835

Zhu C, Sverjensky DA (1992) F-Cl-OH partitioning between biotite and apatite. Geochim Cosmochim Acta 56:3435–3467